FRONT MATTER

Title

- Axially swept dithered light-sheet microscope to reveal cardiac morphology
- AS-DiLS imaging to assess cardiac morphology

Authors

Milad Almasian,[1] Alireza Saberigarakani,[1] Xinyuan Zhang,[1] Jonathan A Brewer,[1] Rayaan Hameed,[2] Jichen Chai,[1] Yangyang Lu,[3] Sarah A. Ware,[4] Shuyue Zhou,[4] Yufeng Wen,[5] Hamza Lalami,[6] Hedyeh Hossein Beigi,[1] Jie Yuan,[1] Jun Liao,[5] Yi Hong,[5] Mingfu Wu,[3] Dan Tong,[4] Darshan Sapkota,[2,6] Yichen Ding[*1,7,8]

Affiliations

[1] Department of Bioengineering, The University of Texas at Dallas, Richardson, TX 75080, USA.
[2] Department of Neuroscience, The University of Texas at Dallas, Richardson, TX 75080, USA.
[3] Department of Pharmacological and Pharmaceutical Sciences, University of Houston, Houston, TX 77204, USA.
[4] Department of Internal Medicine, Division of Cardiology, UT Southwestern Medical Center, Dallas, TX 75390, USA.
[5] Department of Bioengineering, The University of Texas at Arlington, Arlington, TX 76019, USA.
[6] Department of Biological Sciences, The University of Texas at Dallas, Richardson, TX 75080, USA.
[7] Center for Imaging and Surgical Innovation, The University of Texas at Dallas, Richardson, TX 75080, USA.
[8] Hamon Center for Regenerative Science and Medicine, UT Southwestern Medical Center, Dallas, TX 75390, USA.

[*]Corresponding author. Email: yichen.ding@utdallas.edu

Abstract

Understanding cardiac microstructure and vascular networks in their entirety is critical for assessing cardiovascular development, disease progression, and therapeutic interventions. Light-sheet microscopy combined with tissue clearing enables high-resolution volumetric imaging of intact organs but faces limitations in compacted and trabeculated myocardium due to trade-offs among light-sheet thickness, frame rate, and working distance. We developed a quantitative framework that orchestrates illumination-detection dynamics to maintain uniform resolution across multi-scale specimens. Building on this foundation, we implemented high-speed dithered light-sheet (DiLS) illumination, extending the confocal region by at least 40% and enhancing the space-bandwidth product while preserving optical sectioning. Integration of DiLS with an axially swept approach establishes the axially swept dithered light-sheet (AS-DiLS) microscopy, which enhances imaging throughput while preserving axial resolution and enables uniform illumination up to 12.5-millimeter scanning range. AS-DiLS delivers near-isotropic resolution (~2.5 μm) for investigating intricate ventricular trabeculae, pectinate muscles, vasculature, and

extracellular matrix, providing scalable platform for comprehensive cardiovascular morphology and topology assessment from embryonic to adult.

Teaser

Volumetric imaging reveals microstructure and vascular networks in their entirety with near-isotropic resolution.

MAIN TEXT

Introduction

Cardiovascular diseases remain the leading cause of morbidity and mortality worldwide, with their prevalence projected to rise in the future (*1–3*). Cardiac morphology, comprising a complex network of myocardial compaction and trabeculation, vasculature, and extracellular matrix, plays a fundamental role in cardiac function and its adaptability to both physiological and pathophysiological conditions (*4–7*). A comprehensive understanding of cardiac morphology is critical for elucidating the mechanisms underlying cardiac development, remodeling, and aging, ultimately accelerating the development of effective therapeutic interventions. However, high-resolution, whole-volume assessment of cardiac microstructure and vascular network in their entirety still poses substantial technical challenges. In particular, conventional histological approaches often compromise tissue integrity and imaging throughput, while introducing artifacts that misrepresent intricate microstructures and their spatial relationships within the native in situ environment (*8–11*).

While light-sheet microscopy (LSM) has emerged as a powerful modality for volumetric imaging with minimal photodamage (*12–15*), limitations remain in the context of compacted and trabeculated myocardial layers. Specifically, trade-offs in light-sheet thickness, effective range (e.g., confocal region), and imaging speed remain to be addressed in resolving the three-dimensional (3D) cardiac microstructure and vascular network across the entire heart (*16–20*). For instance, a thinner Gaussian beam results in better optical sectioning, but at the cost of a reduced confocal region. While the implementation of extended focusing (*21*) and Bessel beam (*22*) has improved the effective length of the light-sheet, the former leads to range-dependent thickness degradation over the extended scanning field, whereas the latter and its variations come with beam side lobes that compromise imaging fidelity and rely on double- or triple-ring configurations in optimized illumination, which underutilizes the objective's full back aperture. (*23–25*).

To overcome the aforementioned limitations, we developed a quantitative framework that orchestrates illumination and detection dynamics of the light-sheet imaging system to maintain uniform image quality and resolution across the entire imaging plane in multi-scale biological specimens. Through parameter interdependence modeling, this framework enables precise synchronization between illumination and detection, ensuring consistent optical performance across magnifications. Building upon this framework, we introduce a new method termed dithered light-sheet (DiLS), in which the light-sheet is rapidly dithered along its propagation direction which achieves over 40% extension of the confocal region while preserving effective light-sheet thickness compared to conventional Gaussian beam. DiLS can be further integrated with axially swept approaches (*25–27*) through synchronization of the extended focus with the rolling shutter of an sCMOS camera, which excludes nonspecific background outside the effective confocal region. In practical implementation, a voice coil (VC) scanner has been utilized to generate the

DiLS, while axial sweeping has been achieved through an electrically tunable lens (ETL) in the prototype. Our results indicate that the imaging speed of axially swept dithered light-sheet (AS-DiLS) configuration exceeds at least 40% with consistent optical sectioning across the scanning range of up to 12.5 mm, with the improved space-bandwidth product. In combination with tissue clearing (*28*, *29*), AS-DiLS enables near-isotropic spatial resolution of ~2.5 µm throughout the trabeculated myocardium, vascular network, and extracellular matrix in intact hearts. This integrative strategy addresses the issues of photon scattering and optical aberrations caused by heterogeneous refractive indices in densely structured muscles (*29–31*). Our simulation and experimental results confirm the efficacy of the system design, control configuration, and beam profiling across diverse cardiovascular applications.

Collectively, this scheme addresses longstanding challenges in high-resolution analysis of densely structured myocardial architecture, providing significant insights into myocardial and vascular morphology across developmental and disease states from embryonic to adult models. AS-DiLS imaging platform enables precise volumetric mapping of myocardial trabeculae, valves, and vascular networks, facilitating identification of structural defects associated with congenital heart diseases such as left ventricular non-compaction, hypoplastic left heart syndrome, and outflow-tract malformations. By connecting molecular perturbations to whole-organ architecture, it bridges the gap between genotype and phenotype, offering critical structural context needed to define how specific genetic or signaling disruptions manifest as complex congenital malformations.

Results

Standalone DiLS and synchronized AS-DiLS approach

The inherent trade-off between Gaussian beam waist (2ω) and the extent of the confocal region (**Fig. 1A**) imposes limitations on data acquisition speed in axially swept imaging modalities (*25–27*). To enhance optical sectioning and accelerate volumetric imaging within the densely structured myocardium of the intact heart, we sought to generate a time-averaged light-sheet strategy by dynamically dithering the beam waist along its propagation direction. The effective light-sheet thickness is typically accepted as up to $2\sqrt{2}\omega$ for a Gaussian beam profile (*12*, *32*). However, in this case, we used a VC scanner integrated with a remote focusing setup (*33*, *34*) to dither the beam waist along its propagation axis at twice the camera readout rate (e.g., dithering frequency f_{dith} = 2/ET, where ET is exposure time) (**Fig. 1B** and **fig. S1**). Beam profiles of DiLS with varying dithering ranges were captured using 50 µM fluorescein under a 20 ms exposure time and a dithering frequency of 100 Hz (**Fig. 1C**).

The results presented at dithering ranges of 0, 50, 100, and 200 µm revealed notable changes in effective light-sheet thickness (**Fig. 1D**), spatial intensity distribution (**Fig. 1E**), and axial extent of the confocal region (**Fig. 1F**). Using our prototype setup (Plan Fluor 10×/0.3 NA, Nikon), we established a baseline confocal region of 73 µm. To balance thin light-sheet with extended axial coverage, a 100 µm dithering range was identified as optimal in practice (**Fig. 1F**). Under this condition, the effective light-sheet thickness remained below the threshold of $2\sqrt{2}\omega$, varying from 2.57ω to $2\sqrt{2}\omega$ (10.1% relative range), while the corresponding confocal region extended to approximately 105 µm, a 44% improvement over the baseline (**Fig. 1D**). In contrast, a 50 µm dithering range yielded a narrower confocal region of 83 µm and a higher thickness relative range (29.7%, 2.18ω to $2\sqrt{2}\omega$), while a 200 µm range resulted in a beam thicker than $2\sqrt{2}\omega$, falling

outside the preferred region, despite improved intensity uniformity as the dithering range increases (**Fig. 1E**). Simulation results further supported the experimental findings that a 100 µm dithering range is practically optimal (**fig. S2** and **note S1**), and this configuration was adopted for subsequent cardiovascular applications.

To extend the imaging coverage up to centimeter scales, DiLS is able to be integrated with axially swept approaches (*25–27*), enabling a new mode termed AS-DiLS (**fig. S1**). In practice, ETL was added as a secondary scanner into the prototype to axially sweep the dithered beam across the imaging plane, ensuring tight synchronization between the effective confocal region of DiLS and the active pixels of the sCMOS camera (**Fig. 1G**). In AS-DiLS, the camera's exposure time is used to determine the dithering frequency, and the 2D image acquisition time (T_{2D}) is used to derive the axial sweeping frequency (f_{as} = $1/(2\times T_{2D})$) (**note S2** and **equations S1-4**). Briefly, selective pixels (green grid in **Fig. 1H**) are activated upon arrival of the extended beam waist and remain active throughout the exposure period (solid green area), during which they collect signal exclusively from the confocal region (dark blue area). In DiLS, the beam waist dithers back and forth with a period equal to half the exposure time, thereby generating an extended confocal region (light blue area). Compared to LSM with the same exposure time, this extended confocal region in DiLS led to an increased number of active pixels and consequently reduced the line interval time between successive pixel activations (**note S2** and **equations S9-10**), which is an inherent limitation in conventional axially swept modalities. By synchronizing the rolling shutter with the extended beam waist, the reduced acquisition time to generate a 2D frame is defined as follows:

$$T_{2D} = ET\left(\frac{FOV}{CR} - \frac{Px}{CR * M} + 1\right) \#(1)$$

where T_{2D} is the acquisition time of an image, ET is the exposure time, FOV denotes the field of view, CR represents the confocal region, Px refers to the pixel size of the camera sensor, and M is the magnification (**note S3** and **equations S11-12**). Using a 100 µm dithering range, we demonstrated over 40% improvement in imaging speed in AS-DiLS (**Fig. 1H** and **note S3**). Our fluorescein experiments indicated that AS-DiLS achieved a maximum scanning range of 12.5 mm under 1× magnification (**Fig. 1I**). Spatial intensity analysis at the left (0.93 ± 0.02 a.u.), middle (0.94 ± 0.01 a.u.), and right (0.93 ± 0.01 a.u.) regions of the beam showed no statistically significant differences (p = 0.28), indicating uniform beam distribution across the scanning field (**Fig. 1J**).

Characterization of the system

We experimentally characterized system performance under three configurations, LSM, DiLS, and AS-DiLS, all implemented into a single prototype system equipped with a VC scanner and an ETL (*35*) (**fig. S1**). A customized LabVIEW program was developed to synchronize device operations, including the sCMOS camera, VC scanner, and ETL. Additionally, an executive MATLAB script was developed to automate the setup of calculation parameters, including axially swept frequency (f_{as}), dithering frequency (f_{dith}), ETL amplitude, and line interval, ensuring flexible operation and reproducibility across various experimental conditions (**fig. S4**).

The light-sheet beam generated by the cylindrical lens was dithered using the VC scanner at frequencies ranging from 20 to 100 Hz in DiLS, while the extended focus was axially swept using the ETL at frequencies between 0.25 and 2.5 Hz in AS-DiLS. The detection module, consisting of a 1×/0.25 NA objective lens (MV PLAPO, Olympus) and a zoom body (0.63–6.3×, MVX-ZB10, Olympus), provides a long working distance of 87 mm and

a flexible FOV from 21 mm to 2.1 mm. This design addresses constraints associated with working distance for intact rodent hearts, reduces challenges posed by refractive index matching solutions, streamlines multi-immersion protocols for tissue-cleared samples within the imaging chamber, and leverages the extended depth of field via spherical aberration correction (*36*).

Spatial resolution was assessed using 0.53 µm fluorescent beads. Under the LSM configuration, the minimum axial resolution at the beam waist was 2.24 µm. Consequently, the confocal region, defined as the range where axial resolution remains below 3.15 µm was measured to be 73 µm. The lateral resolutions (in blue) of three representative beads located to the left, within, and to the right of the confocal region were 2.31 µm, 2.25 µm, and 2.11 µm, respectively, while the axial resolutions (in red) were 6.09 µm, 2.69 µm, and 6.87 µm, respectively, indicating the varying light-sheet thickness along the propagation direction (**Fig. 2A** and data for all beads in **figs. S5A-B**). Within the confocal region, the lateral resolution of all beads (n = 103) was 2.25 ± 0.08 µm along the x-axis and 2.79 ± 0.13 µm along the y-axis, with an average axial resolution of 2.63 ± 0.30 µm.

Under DiLS conditions with ET = 20 ms and f_{dith} = 100 Hz, the lateral resolutions of the same representative beads were 2.48 µm, 2.22 µm, and 2.49 µm, respectively, while the axial resolutions were 5.42 µm, 2.22 µm, and 6.46 µm, respectively (**Fig. 2B** and data for all beads in **figs. S5C-D**). Using the same threshold of 3.15 µm as in LSM, the extended confocal region was determined to be 103 µm (41% improvement). Within this region, the mean lateral resolutions (n = 115) were 2.49 ± 0.32 µm along the x-axis and 2.77 ± 0.19 µm along the y-axis, with an average axial resolution of 2.91 ± 0.16 µm. In comparison, AS-DiLS yielded lateral resolutions of 2.22 µm, 2.79 µm, and 2.47 µm, and axial resolutions of 2.39 µm, 2.48 µm, and 2.65 µm. Measurements of two additional beads located at the extreme left and right of the FOV indicated lateral resolutions of 2.49 µm and 2.17 µm, and axial resolutions of 2.25 µm and 2.76 µm, respectively. Comprehensive analysis of all resolved beads (n = 1579) captured by AS-DiLS revealed lateral resolutions of 2.42 ± 0.24 µm (x-axis) and 2.65 ± 0.18 µm (y-axis), and an axial resolution of 2.68 ± 0.25 µm, across 1.8 mm at 6.3× zoom magnification (**Fig. 2C**). Importantly, AS-DiLS maintained this near-isotropic resolution across an FOV that was 25 times larger than that of conventional LSM. As a result, the space–bandwidth product (FOV/Resolution^2), a qualitative metric for assessing an image's information-carrying capacity, is therefore enhanced (*37*). These results demonstrate that AS-DiLS achieves near-isotropic resolution and consistent optical sectioning throughout the entire scanned range. In addition, the coefficient of variation (CV) was utilized to quantify the relative variability in axial resolution across the three configurations. Our results showed that CV values of 11% for LSM (n = 103), 5.5% for DiLS (n = 115), and 9.3% for AS-DiLS (n = 1579), indicating that the axial performance of both DiLS and AS-DiLS outperforms that of LSM within the confocal region.

Assessment of image quality in hearts

Significant light attenuation primarily caused by fibrous tissue and heterogeneous refractive indices within the densely structured myocardium consistently degrades the image quality in conventional volumetric imaging of intact hearts. Our methodology is compatible with multiple established tissue clearing methods, most notably iDISCO for demonstration in this study (*28*, *38*). Prior to imaging, cardiac specimens were cleared and embedded in 1% agarose gel and filled with the refractive index-matching solution for

imaging by either autofluorescence or immunolabeling (**Figs. 3A-B**). To evaluate the consistency of structural information across the entire imaging plane in AS-DiLS, a cleared mouse heart was translated laterally in six increments of 341 µm, with an image acquired at each position under the same imaging conditions (**Fig. 3C**). The selected region of interest (341 × 2048 µm) was assessed across six sequential images using the structural similarity index measure (SSIM). With values ranging from 0.96 to 0.99, the analysis revealed a high degree of similarity between adjacent regions, indicating that the optical sectioning capability of AS-DiLS is spatially independent and effectively preserves physiological structural information (**Fig. 3D**).

To further assess AS-DiLS performance in the heterogeneous cardiac tissues, three representative regions (1 × 1 mm) of the mouse heart were selected along the light-sheet propagation axis: the distal (green), the confocal region (orange), and the proximal ends (purple) (**Fig. 3E** and **table S1**). AS-DiLS consistently revealed the myocardial microstructures across three sections spanning over 5 mm, in contrast to the degraded image quality at both ends when AS-DiLS was disabled (**movie S1**). Quantitative analysis indicated that activating AS-DiLS increased the signal-to-background ratio (SBR) by 13.8% (from 5.8 to 6.6), 5.3% (from 7.6 to 8.0), and 10.9% (from 9.2 to 10.2) in the distal, confocal, and proximal regions, respectively. Similarly, contrast-to-noise ratio (CNR) improved by 23.7% (from 97.4 to 120.5), 14.3% (from 132.1 to 151.0), and 20.7% (from 164.0 to 198.0) across the same regions, affirming robust signal and contrast enhancement throughout heterogeneous, densely structured myocardial tissue using AS-DiLS (**Fig. 3F**). Image sharpness, assessed by the first derivative of intensity profiles, increased 2.1-fold and 3.1-fold at the distal and proximal ends, respectively, while remaining ~1.1-fold within the confocal region (**Fig. 3G**), demonstrating improved optical sectioning capability outside the confocal region with AS-DiLS. Our Fourier analysis further revealed the optical transfer function (OTF) cut-off radius, which represents the lower-bound estimate of supported frequencies (*39*), increased by 8%, 12%, and 35% in the distal, confocal, and proximal regions, respectively, indicating improved capture of fine structural details enabled by AS-DiLS (**Fig. 3H** and **fig. S9**).

Morphological analysis of the cardiac specimens

To demonstrate whole-heart imaging capability, we implemented AS-DiLS into the autofluorescence imaging of myocardium from mouse embryos to neonates to adults. To cover an intact adult mouse (14 months, male, C57BL, The Jackson Lab), we stitched three consecutive AS-DiLS tiles with a 10% overlap along the ventricular long axis. The entire image stack includes a volumetric region measuring 5.3 × 9 × 5 mm^3, with an acquisition time of approximately 35 min per tile for 961 images, and a total data size of 13.3 GB (**Fig. 4A** and **table S1**).

The representative myocardial section along the long axis (depth = 2350 µm) (**Fig. 4B**) and the 3D rendering (**Fig. 4C**) provided an entry point to investigate myocardial architecture at both the global pattern and regional detail levels. These include the pectinate muscle in atria, myocardial fibers, papillary muscle, and trabecular network in ventricles, aortic valve leaflet associated with the ascending aorta, and coronary arteries throughout the heart (Insets in **Fig. 4C** and **movie S2**). The near-isotropic resolution enables quantitative analysis of well-resolved microstructure from physiologically relevant perspectives, such as long- and short-axis views, after volumetric rendering. For instance, our results revealed that the average thickness of a representative myocardial fiber, measured at 10 points, was 23.6 ± 3.6 µm (**Fig. 4C, middle**). The wall thickness of

the left coronary artery and ascending aorta were 18.4 ± 4.9 μm and 118.5 ± 5.5 μm, respectively, with the lumen area of 8.8 × 10□ μm² (**Fig. 4C, bottom**), consistent with other 2D measurements (*40*, *41*).

In addition to myocardial microstructure, this scheme also enables detailed morphological analysis of vasculature. We extracted the coronary arteries by tracing and segmenting the vessels from their aortic origins to distal branches. The binarized left coronary artery (LCA), septal artery (SpA), and right coronary artery (RCA) were digitally traced to identify vessel centerlines, branching points, and local lumen diameters (**Fig. 4D** and **movie S3**) (*42*). Morphological analysis reveals fourth-order vessel branch counts of 411, 141, and 69 for the LCA, SpA, and RCA, respectively, with corresponding mean diameters of 13.4 ± 6.2 μm, 10.4 ± 4.4 μm, and 13.3 ± 4.9 μm. Beyond global averaging, spatially resolved analysis of the LCA enables visualization of localized diameter variation ranging from ~3 μm to 50 μm, capturing fine-detail vessel heterogeneity along its vascular tree (**Fig. 4E** and **movie S4**).

Our scheme also enables high-resolution study of the extracellular matrix, a key contributor to cardiac integrity, mechanical behavior, and overall function (*43*, *44*). Following decellularization and tissue clearing, AS-DiLS was employed for autofluorescence imaging of intact adult rat hearts using three stitched tiles (**Fig. 4F** and **movie S5**), as well as for imaging of a representative section from the porcine left ventricular wall (**Fig. 4G** and **movie S6**). To assess regional variability in the adult rat heart, extracellular volume (ECV) fractions were quantified within three 330 × 330 × 500 μm^3 volumes in the left ventricular wall (LVW), right ventricular wall (RVW), and interventricular septum (IVS), yielding values of 0.32, 0.33, and 0.26, respectively. This volumetric analysis provides a foundation for characterizing extracellular matrix organization under physiological conditions and offers a framework for future investigations into pathological remodeling processes, such as fibrosis and heart failure (*45*, *46*).

Topological analysis of vascular network

Specific fluorescence labeling can be effectively integrated into existing imaging and clearing strategies. We investigated the vasculature of intact neonatal mouse hearts using in vivo CD31 labeling. To specifically trace the vascular network in deep tissue, three neonatal mouse hearts at postnatal day 7 (P7) were labeled with CD31 antibody via retro-orbital injection, then fixed in paraformaldehyde at 1-, 2-, and 18-hour post-injection, followed by tissue clearing and imaging for approximately 45 min (**fig. S10** and **table S1**). AS-DiLS resolves the extensive vascular network, including coronary arteries and microcirculatory networks, in fine detail and contrast deep inside the heart at a depth of 960 μm (**Figs. 5A-B**), supporting the quantification of endothelial layer thickness in the LCA of 11.89 μm along the long axis and 12.47 μm along the short axis. We traced the delineated vascular network in LCA and SpA from their aortic origins to distal branches throughout the intact heart, revealing branching patterns and continuous microvasculature down to fifth-order vessel branches (**Fig. 5C** and **movies S7-8**). Importantly, this method not only reveals vascular connectivity, but also facilitates assessment of patency among dense microcirculatory networks, supporting the analysis of vascular injury and remodeling in further studies (*47*). To assess microcirculatory features in 3D, we applied Frangi vesselness filtering and filament tracing to reconstruct the capillary network. From each heart, a total of nine representative sections (200 × 200 × 400 μm^3) were selected from LVW, RVW, and IVS, three from each region, for vessel length density (VLD)

quantification (**Fig. 5D**). Our statistical analysis of VLD across LVW, RVW, and IVS sections suggests no statistically significant difference among these regions.

In addition to in vivo CD31 labeling, whole-mount immunostaining of vasculature was performed in mouse embryos at E14.5, E15.5, and E16.5, followed by AS-DiLS imaging (**Fig. 5E**). This method enables labeling and spatial mapping of the vascular network across the entire heart, allowing imaging through the full 2.2-mm depth of the embryonic heart. The segmented vasculature was converted into graph representations for topological analysis using Euler characteristic (χ) and clustering coefficient (*48*, *49*). Enumeration of graph features, including branching points, vessels, and closed loops of the vascular network, enabled interpretation of network architecture, in which higher χ values reflect a sparse, tree-like structure, whereas lower values suggest greater interconnectivity and vascular redundancy. From four representative $260 \times 260 \times 260\ \mu m^3$ volumes per heart, the mean Euler characteristics were $\chi = -27.5 \pm 11.4$ for E14.5, $\chi = -27.3 \pm 4.1$ for E15.5, and $\chi = -65.8 \pm 9.8$ for E16.5.

In addition, local vascular connectivity was further assessed using the clustering coefficient (C_i), which quantifies the degree of interconnectivity among neighboring nodes within the vascular graph. For each node, C_i is defined as the ratio of the number of observed connections between its neighboring nodes to the total number of possible connections among those neighbors (*48*, *49*). This metric provides insight into localized network organization, in which higher C values suggest denser, more interconnected vascular substructures, while lower values indicate sparser configurations. Analysis of these coefficients across developmental time points revealed changes in microvascular architecture, complementing the global topological trends observed in the Euler characteristic. Global clustering coefficients, calculated from local C_i values across four volumes from three hearts, were $C = (3.3 \pm 2.3) \times 10^{-2}$ for E14.5, $C = (5.0 \pm 2.3) \times 10^{-2}$ for E15.5, and $C = (5.2 \pm 1.5) \times 10^{-2}$ for E16.5, suggesting intense angiogenesis to meet the elevated metabolic demands during this stage of heart development. Collectively, the morphological and topological analyses enabled by AS-DiLS advance our understanding of myocardial microstructure and vasculature in the intact heart with improved speed and space-bandwidth product. This integrated approach holds great promise for facilitating comprehensive and multi-scale assessment of cardiovascular development, pathological remodeling, and therapeutic response, providing an entry point for further investigations into cardiac function and disease progression.

Discussion

Advanced understanding of cardiac morphology is crucial for new insights into heart development, regeneration, protection, and aging, ultimately allowing for new therapeutic strategies for diseases such as cardiomyopathy. However, investigation of both global patterns and local details of cardiac microstructures, including myocardial trabeculation, myofibers, valve leaflets, vasculature, and extracellular matrix, remains technically challenging. To address this issue, we have developed the AS-DiLS imaging scheme, which enables comprehensive volumetric analysis of intact ventricles and atria at micrometer-scale resolution. By harnessing the intrinsic autofluorescence of myocardial tissue, our method provides sufficient contrast to delineate cardiac architecture and coronary arteries for both macro- and micro-scale assessments. Furthermore, the integration of specific immunolabeling with tissue clearing approaches facilitates full mapping of the vascular network across the entire heart from embryos to neonates. Complementing this, computational analysis of the imaged cardiac tissue enables

quantitative assessment of anatomical features such as muscle fibers, chambers, extracellular matrix, and vasculature, revealing volumetric relationships that are inaccessible through conventional imaging approaches. In combination with computational fluid dynamics, these datasets further allow investigation of flow capacity and hemodynamics (*50*, *51*).

The DiLS scheme offers notable flexibility, operating either as a standalone system or in combination with axial sweeping techniques. The integration of DiLS in axial sweep approach enables an extended propagation range of up to 12.5 mm, while enhancing imaging speed by over 40% and maintaining uniform optical sectioning and intensity. The system also supports stitching and multiview imaging strategies to expand FOV, achieving 2.5 µm near-isotropic resolution. Uniform optical sectioning and intensity in the time-averaged light-sheet are achieved by synchronizing rapid laser dithering with line intervals within a single camera exposure. When the dithering frequency is set to an integer multiple of the camera readout rate, the beam waist scans each pixel an equal number of times. In our implementation, the dithering frequency was set to twice the inverse of the exposure time, constrained by the operational limits of the VC scanner. Future integration of high-speed scanners with closed-loop feedback control holds promise for further improving imaging speed. Moreover, optimizing the dithering frequency enables a tunable balance between light-sheet thickness and scanning velocity. The resulting expansion of the confocal region and improved data acquisition rate, modulated by dithering frequency, make the DiLS scheme highly adaptable for a broad range of imaging applications. Beyond dithering frequency optimization, the AS-DiLS scheme could be further improved using multiple foci generated by other devices like digital micro-mirrors (*52*), spatial light modulator (*53*), and multilayer beam splitter (*54*). Additionally, to correct for the Gaussian distribution of laser intensity along the light-sheet height, a galvanometer-based laser scanning or Gaussian blur-based post-processing could be employed to achieve evenly distributed illumination, thereby improving uniformity across the imaging volume.

Regarding image quality, the current limitation in pixel size on the sCMOS camera presents a fundamental challenge for digital sampling. Although the theoretical optical resolution of our system approaches ~1 µm, it is constrained by a maximal digital sampling rate of 1 µm under 6.3× magnification. To overcome this limitation, our subvoxel sampling techniques (*37*, *55*) offer promising resolution enhancement through sequential subvoxel shifting mechanisms, thereby increasing the system's space-bandwidth product. One key advantage of the AS-DiLS scheme is its ability to suppress stripe artifacts, which in conventional LSM arise from photon scattering and absorption. These artifacts are minimized in AS-DiLS by dynamic focus dithering and sweeping (**Fig. 3E** and **fig. S9**). Additionally, to mitigate the decline in SBR and CNR observed in densely layered cardiac tissues at the distal end of light propagation, multi-directional illumination or multiview fusion (*56*, *57*) strategies could be incorporated. These approaches have the potential to collectively improve image fidelity and extended imaging depth, making AS-DiLS a robust platform for high-resolution volumetric imaging of intricate microstructure under physiological and pathophysiological conditions.

Parallel advances in open-top imaging system designs (*58–60*), deep learning tools (*61*, *62*), and extended reality (*63–66*) offer complementary opportunities for feature extraction and interpretation of complex microstructures within the cardiovascular system and 3D cell cultures. The use of specific fluorescence labeling, either immunostaining or transgenic reporter lines, further enhances the efficiency and scalability of high-

throughput analysis. Collectively, the ongoing integration of technical advances with extensively established animal models and human-derived cell cultures is poised to bridge current knowledge gaps and accelerate discovery in cardiovascular research. This convergence will yield deeper insights into cardiac morphology and function, ultimately paving the way for novel preventive and therapeutic strategies.

Materials and Methods

System design

This in-house system integrates three configurations: conventional LSM, DiLS, and AS-DiLS (**fig. S1**). It consists of three continuous-wave diode-pumped solid-state lasers with wavelengths of 473 nm, 532 nm, and 589 nm (LRS-0473-PFM-00100-05, LRS-0532-PFM-00100-05, LRS-0589-GFF-00100-05, Laserglow Technologies). The diameter of laser beams was controlled using a 10× achromatic beam expander (GBE10-A, Thorlabs) and an iris (ID20/M, Thorlabs). A remote focusing design including a VC flexure scanner (VCFL35, Thorlabs), a half-wave plate (AHWP3, Bolder Vision Optik), a polarizing beam splitter (CCM1-PBS251/M, Thorlabs), a quarter-wave plate (AQWP3, Bolder Vision Optik), and an objective lens (Plan Fluor 10×/0.3 NA, Nikon) (*33*, *34*) was implemented to generate the DiLS in the illumination path. The beam reflected from the VC scanner was focused using a plano-convex cylindrical lens (f = 50 mm, ACY254-050-A, Thorlabs) to form a light sheet. The ETL (EL-16-40-TC, Optotune) was vertically mounted on the focal plane of the cylindrical lens to axially sweep the dithered beam, serving as the second scanner in AS-DiLS. A series of achromatic doublets (f_1 = 100 mm, f_2 = 60 mm, AC254-100-A, AC254-060-A, Thorlabs) and the objective lens (Plan Fluor 10×/0.3 NA, Nikon) were used to relay and reshape the beam into a vertical light-sheet in the imaging plane.

The detection module was built upon our established LSM system (*35*) that includes an objective lens (1×/0.25 NA, MV PLAPO, Olympus), a zoom body (0.63–6.3×, MVX-ZB10, Olympus), a filter wheel (LB10-W32, Sutter Instrument), a set of filters (ET525-30, ET585-40, ET645-75, Chroma), a tube lens (MVX10, Olympus), and an sCMOS camera (Flash 4.0 v3, Hamamatsu). The entire detection module was mounted on a high-precision translational stage (C-884.4DC, Physik Instrumente) to align the detection focus with the light-sheet.

A custom-designed chamber was 3D-printed to isolate the tissue clearing solution from the detection lens, providing a uniform refractive index environment, leveraging the extended depth of field, and ensuring compatibility with multiple clearing protocols (*36*). For precise positioning, we used a 4D motorized stage that includes 3D translational movement (L-406.20DG10, L-406.40DG10, M-403.4PD, controller C-884, Physik Instrument) and 1D rotation (1474 stepper motor, Pololu).

System control

A customized control algorithm developed in LabVIEW (2017 SP1, National Instruments), along with NI VAS (20.0), compactRIO (20.0), FlexRIO (20.0), R-series (20.0), Serial (20.0), DAQmx (20.1), and a DAQ card (PCIe-6363, National Instruments), was utilized to enable the system synchronization. To enable smooth translation of the VC scanner, a filtered triangular waveform was generated via the NI card, amplified through a TI module (OPA548EVM, Evaluation Module, Texas Instruments), and powered by a 3-

channel supply unit (T3PS43203, Teledyne LeCroy) (**figs. S11-12**). Axial sweeping was achieved at a constant velocity using an ETL driven by an independent triangular trigger ranging from 0.25 to 4 Hz, with a 2.5 V offset and an amplitude of 0 to 2.5 V (**fig. S13**). We diagnosed synchronization errors by rotating the camera 90°, aligning the rolling shutter vertically against the light-sheet sweep. Ideal synchronization produced a diagonal line, indicating precise matching of ETL scanning and shutter activation (**figs. S14-15**). Image acquisition on the sCMOS camera was triggered by an edge signal from the NI card, and an empirically determined 8 ms phase delay was introduced to synchronize the ETL with the camera (**fig. S16**). In AS-DiLS, the exposure time serves as the primary control parameter, from which the line interval and the corresponding dithering and sweeping frequencies are derived. The line interval also governs the rolling shutter speed, ensuring precise temporal coordination between active pixel rows and the beam waist (**notes S2-3**).

Image rendering

Image stitching was performed to reconstruct the adult heart dataset. Individual 16-bit TIFF files were imported into the BigStitcher plugin in Fiji (version 1.54f) for stitching and fusion (*67–69*). Datasets exceeding 5 GB were downsampled using 2× binning and converted into 8-bit images in Fiji for 3D rendering in Amira (2021.2; Thermo Fisher Scientific) (*42*).

Simulation of static and dithered light-sheet

A static Gaussian light-sheet was synthesized using the Fourier transform and angular spectrum propagation methods to obtain its cross-sectional intensity profile. In the spatial frequency domain, the illumination beam was described as:

$$E(f_z) = \exp\left(\frac{-{f_z}^2}{(\tau f_0)^2}\right) \#(2)$$

where τ is a shape parameter that controls beam thickness ($\tau = 0.08$), and $f_0 = n/\lambda$ is the characteristic spatial frequency determined by the refractive index ($n = 1.33$) and wavelength ($\lambda = 532$ nm). The inverse Fourier transform of $E(f_z)$ was used to obtain the axial field distribution at the focal plane, corresponding to the light-sheet waist. The field was propagated using the angular spectrum method to obtain its evolution along the propagation axis. The light-sheet intensity distribution was then obtained as the squared magnitude of the complex field. In the dithered configuration, the Gaussian light-sheet was rapidly dithered along the propagation axis, and its effective profile was defined by the time-averaged intensity. At each spatial position, the time-averaged intensity was calculated by integrating the instantaneous field intensity over a dithering period (Δt). The total displacement during one cycle was $v \times \Delta t$, corresponding to twice the dithering amplitude. For both static and dithered light-sheet, the thickness was defined as the full width at half maximum (FWHM) of the intensity profile at the waist.

Point spread function calibration

Fluorescent beads (0.53 µm, FP-0556-2, Spherotech) were diluted to a concentration of $1{:}1\times10^5$ in a 1% low-melting point agarose solution (16520050, Thermo Fisher Scientific). They were mounted in a fluorinated ethylene propylene tube and placed in a chamber filled with double-deionized water for imaging. The point spread function of each bead was analyzed by fitting a Gaussian distribution to determine the FWHM. All resolved beads across the entire volume were analyzed in MATLAB (*70*).

Beam profile test

A 50 µM fluorescein solution was utilized to record the beam profile. It was prepared by dissolving 3 mg of fluorescein in 180 mL of deionized water, followed by mixing with 20 mL of 10× phosphate buffered saline (PBS) in the imaging chamber. To capture the beam profile, the cylindrical lens was replaced with an achromatic doublet lens of identical focal length (AC254-050-A, Thorlabs) (*70*).

Animal specimens

All animal protocols, experiments, and housing described in this manuscript were approved by the Institutional Animal Care and Use Committee (IACUC #20-07 and #21-03) of the University of Texas at Dallas and other institutions from which the samples were obtained.

Tissue clearing

All hearts were cleared under the iDISCO protocol (*28*, *38*). Fixation was performed in 4% paraformaldehyde, adult hearts for 18 hours, embryonic hearts for 2 hours, and three neonatal hearts for 1, 2, and 18 hours, respectively. Following fixation, hearts were rinsed three times in 1× PBS for 30 min each. These samples were then dehydrated at room temperature by agitating in methanol with increasing concentrations (20%, 40%, 60%, 80%, and 100%), each for 1 hour. Delipidation was carried out by overnight immersion in dichloromethane at room temperature, followed by two 30-min washes in methanol. Hearts were bleached in 5% H_2O_2 in methanol overnight at 4°C. These samples were rehydrated through a reverse methanol gradient (100%, 80%, 60%, 40%, and 20%) and finally in 1× PBS at room temperature, each for 1 hour. To enhance permeability, hearts were washed twice in 0.2% Triton X-100 in 1× PBS at room temperature for 1 hour. Embryonic and neonatal hearts were ready for optional immunolabeling. Subsequently, hearts were embedded in a 1% agarose prepared in 1× PBS. They were dehydrated again in methanol with increasing concentrations (20% to 100%) for 1 hour each, followed by immersion in a 66% dichloromethane / 33% methanol mixture at room temperature for 3 hours to complete lipid removal and allow the samples to sink. Finally, hearts were submerged in dibenzyl ether until fully transparent.

In vivo CD31 immunolabeling

Neonatal mice P7 were anesthetized by isoflurane. Each mouse then received a retro-orbital intravenous injection (*50*, *71*) of 20 µL rat anti-mouse CD31 antibody conjugated to Alexa Fluor 594 (102520, BioLegend), diluted 1:5 in 1× PBS. After the injection, the mice were returned to their mother for 30 min prior to euthanasia. The hearts were then perfused with 2 mL of 4°C 1× PBS through the left ventricle. Hearts were harvested and placed into 4°C 1× PBS and gently compressed with flat-tip forceps to remove residual blood. Following the iDISCO protocol, the hearts were blocked in a solution containing 10% dimethyl sulfoxide (DMSO) and 6% normal donkey serum (NDS; 017-000-121, Jackson ImmunoResearch) in 0.2% Triton X-100 for 2 days at 37°C for immunolabeling. Alexa Fluor 594-conjugated secondary antibodies (712-585-153, Jackson ImmunoResearch) were diluted 1:1 in 1× PBS containing 3% NDS, 0.2% Tween-20, and 0.1% heparin and the hearts were immersed for 7 days at 37°C. The hearts were then washed every 1 hour in 1× PBS containing 0.2% Tween-20 and 0.1% heparin (H4784-1G, Sigma) five times, followed by an overnight wash. Finally, the samples were cleared using the remaining steps of the iDISCO protocol.

Immunolabeling in the embryonic heart

Embryonic mouse hearts were immunolabeled following iDISCO protocol. 2.5 µL of 1% biotin-conjugated Cholera Toxin Subunit B was injected slowly. Hearts were incubated in a permeabilization solution containing 0.2% Tween-20 and 0.1% heparin in 1× PBS for 2 days at 37°C in a water bath. Following permeabilization, samples were blocked in a solution of 20% DMSO, 0.2% glycine, and 0.2% Triton X-100 for 2 days at 37°C. A second blocking step was performed in 10% DMSO and 6% serum in 0.2% Triton X-100 for an additional 2 days at 37°C. For primary antibody incubation, PECAM and Endomucin were diluted in 1× PBS containing 5% DMSO, 3% NDS, 0.2% Tween-20, and 0.1% heparin, and incubated with the samples for 7 days at 37°C. Following primary labeling, hearts were washed five times in PBS containing 0.2% Tween-20 and 0.1% heparin for 1 hour each, followed by an overnight wash. Secondary antibody incubation was carried out using Alexa Fluor 568, diluted in PBS with 3% NDS, 0.2% Tween-20, and 0.1% heparin. Hearts were incubated for 7 days at 37°C. Post-secondary incubation, hearts were washed five times in PBS containing 0.2% Tween-20 and 0.1% heparin for 1 hour each, followed by an overnight wash. Finally, immunolabeled hearts were cleared using the remaining steps of the iDISCO protocol.

Vessel segmentation, tracing, and quantification

Manual segmentation of the coronary artery lumen in the adult mouse heart was performed based on the geometry and intensity difference between the vessel wall and the lumen area. Segmentation started at the origin of the left, right, and septal coronary arteries at the aorta and continued to the fully resolved vessel branches, using 2D cross-sectional images. To quantify local vessel morphology, filament tracing was conducted to convert the segmented volume into a graph-based representation. The centerlines were extracted to compute geometric features, including the number of vessel branches (edges), branching points (nodes), and local radii. The radius along the centerline was calculated based on the minimum distance to the vessel boundary, assuming a circular cross-section. The spatial variations of local lumen radius throughout the coronary network were visualized in a 3D color-coded map, where the smallest radii were shown in blue and the largest radii in red. VLD was calculated by cropping 200 × 200 × 400 µm sub-volumes from whole-heart image stacks. The cropped stacks were denoised by applying Gaussian smoothing (σ = 1 µm), followed by background subtraction with a rolling ball radius of 20 µm. A Frangi vesselness filter (*72*, *73*) was applied to enhance vessel contrast and improve continuity, particularly for capillaries. The processed image stack was used for subsequent analyses.

Extracellular matrix sample preparation

Decellularized extracellular matrix of rat and porcine hearts was prepared following adapted protocols (*74*, *75*). The left ventricle of adult porcine hearts (Animal Technologies, Inc.) was dissected, and excess vasculature, adipose tissue, and connective tissue were removed. The isolated myocardium was sectioned into ~1 mm thick sections and rinsed extensively with deionized water to remove residual blood. Tissues were decellularized in 1% sodium dodecyl sulfate (SDS) solution for 4 days at room temperature, with daily replacement of fresh SDS, followed by an overnight rinse in deionized water to remove residual detergent. The rat heart was harvested from a euthanized Sprague-Dawley rat via thoracotomy. After removing adipose and connective tissue, the heart was decellularized in 1% SDS solution for 3 weeks at room temperature. Fresh SDS was replaced daily during the first week and every other day thereafter to ensure effective detergent exchange. To enhance tissue permeability, 1% SDS was injected twice daily through the aorta using a syringe. Upon completion of detergent treatment, hearts were rinsed thoroughly in

excess deionized water for 24 hours to remove residual SDS. The decellularized tissues were dehydrated and rehydrated using the iDISCO protocol to prepare them for imaging.

Coefficient of variation

The CV, defined as the ratio of the standard deviation (σ) to the mean (μ) of the measured FWHM, was calculated to assess the uniformity of resolution:

$$CV = \frac{\sigma}{\mu} * 100 \#(3)$$

CV values less than 10% were considered acceptable uniformity in this study.

Contrast-to-noise ratio and signal-to-background ratio

The CNR and SBR were calculated as follows, respectively (*76*):

$$CNR = \frac{\mu_S - \mu_{BG}}{\sigma_{BG}} \#(4)$$

$$SBR = \frac{\mu_S}{\mu_{BG}} \#(5)$$

where μ_S is the mean intensity of fluorescence measured within the region of interest, μ_{BG} is the mean intensity of the background, and σ_{BG} indicates the standard deviation of the background intensity. Higher CNR values indicate a clearer distinction between the fluorescence signal and background, whereas higher SBR values reflect a greater proportion of fluorescence photons relative to background photons.

Fourier transform analysis

Image quality improvement from LSM to AS-DiLS was quantified by estimating the ratio of OTF support radii between two images from the same region (*39*). Fourier power spectra were obtained by applying the Fast Fourier Transform to both the AS-DiLS image and LSM image. Edge effects were removed by applying a Hanning window, and signal power was isolated using background power subtraction, both ensuring accurate and consistent OTF support radii estimation. The cut-off radius used to quantify image quality improvement was determined through radial projections of the Fourier spectra, determined by the maximum projection length before falling below a power threshold of 1%:

$$F(\mathrm{AS-DiLS}) = \max\left\{r \middle| R(\mathrm{AS-DiLS})_r > \left(\alpha \max_r\{R(\mathrm{AS-DiLS})_r\}\right)\right\} \#(6)$$

Repeating these steps for LSM image, then comparing the ratio of the OTF support radii (*F*(AS-DiLS) / *F*(LSM)) quantifies relative image improvement, where values greater than 1 indicate enhanced image quality and resolution in AS-DiLS image. This method supplements spatial analysis by providing insights into the frequency relationships affecting imaging system parameters, particularly in complex biological tissues, where point-emitter-based OTF measurements cannot be implemented. To eliminate the effect of horizontal stripes in LSM imaging during Fourier transform analysis, artifacts observed along the k_y-axis in the Fourier domain were removed using frequency-domain filtering.

Topological analysis of the vascular network

The Euler characteristic (χ), a global topological metric reflecting the balance between branching, connectivity, and looping of the network (*48*), was used to quantify the overall shape and connectivity of the vasculature, and is defined as:

$$\chi = V - E + F \#(7)$$

where *V* is the number of branching points or endpoints, *E* is the number of vessel segments, and *F* is the number of closed-loop vessels. A high value indicates a simpler,

tree-like structure with less interconnectivity, whereas a low value suggests a more complex and interconnected vascular architecture (*77*).

To assess local connectivity within the vascular network, the clustering coefficient was calculated as a measure of the tendency for branching points to form interconnected neighborhoods. For each node, the local clustering coefficient C_i was computed based on the number of actual connections between its neighboring nodes relative to the total possible connections among them, and is defined as:

$$C_i = \frac{2\, e_i}{k_i\,(k_i - 1)} \quad \#(8)$$

where e_i is the number of edges between the k_i neighbors of node i, and $k_i(k_i - 1)/2$ represents the total number of possible connections among neighbors of node i (*78*). A higher clustering coefficient indicates a more interconnected local neighborhood.

The global clustering coefficient, defined as the average of local coefficients across all branching points, was calculated as:

$$C = \frac{1}{n}\sum_{i=1}^{n} C_i \quad \#(9)$$

where C is the global clustering coefficient, and n is the number of branching points.

Structural similarity index measure

The SSIM was employed to assess the consistency of structural information during the axial sweeping across the imaging plane, and is defined as (*79*):

$$SSIM(a,b) = \frac{(2\mu_a\mu_b + D_1)(2\sigma_{ab} + D_2)}{(\mu_a^2 + \mu_b^2 + D_1)(\sigma_a^2 + \sigma_b^2 + D_2)} \quad \#(10)$$

where μ_a and μ_b are the mean intensities of images a and b; σ_a^2 and σ_b^2 are the variances of images a and b; σ_{ab} is the covariance between two images; D_1 and D_2 are the variables used to stabilize the division with a small denominator, and are determined as: $D_1 = (0.01 \times L)^2$, $D_2 = (0.03 \times L)^2$, where $L = 2^{16}-1$ for 16-bit images.

Statistical analysis

All data are presented as mean ± standard deviation. Statistical analysis was performed using one-way ANOVA for comparisons among multiple groups. For pairwise comparisons, unpaired two-tailed Student's t-tests were used. Differences were considered statistically significant at $p < 0.05$.

Workstations

Images were collected by a dedicated workstation equipped with a processor (Xeon W-2245, 3.9 GHz, 8 Core, Intel), a graphics card (Quadro RTX 4000, NVIDIA), and 256 GB of RAM. The motherboard houses several PCIe cards, including 2 CameraLink frame grabbers for streaming images from the camera, and a DAQ card (PCIe-6363, National Instruments) for generating analog output voltages. For image post-processing, computational analysis, and rendering, a workstation equipped with a processor (Xeon Gold 6258R, 2.69 GHz, 56 Core, Intel), two graphics cards (RTX A6000 GPU, NVIDIA), and 770 GB of RAM was used.

References

1. GBD 2019 Risk Factors Collaborators, Global burden of 87 risk factors in 204 countries and territories, 1990–2019: a systematic analysis for the Global Burden of Disease Study 2019. *Lancet* **396**, 1223–1249 (2020).

2. S. S. Martin, A. W. Aday, N. B. Allen, Z. I. Almarzooq, C. A. M. Anderson, P. Arora, C. L. Avery, C. M. Baker-Smith, N. Bansal, A. Z. Beaton, Y. Commodore-Mensah, M. E. Currie, M. S. V. Elkind, W. Fan, G. Generoso, B. B. Gibbs, D. G. Heard, S. Hiremath, M. C. Johansen, D. S. Kazi, D. Ko, M. H. Leppert, J. W. Magnani, E. D. Michos, M. E. Mussolino, N. I. Parikh, S. M. Perman, M. Rezk-Hanna, G. A. Roth, N. S. Shah, M. V. Springer, M.-P. St-Onge, E. L. Thacker, S. M. Urbut, H. G. C. Van Spall, J. H. Voeks, S. P. Whelton, N. D. Wong, S. S. Wong, K. Yaffe, L. P. Palaniappan, 2025 Heart Disease and Stroke Statistics: A Report of US and Global Data From the American Heart Association. *Circulation* **151**, e41–e660 (2025).
3. S. de Bell, Z. Zhelev, A. Bethel, J. T. Coon, R. Anderson, Factors influencing effective data sharing between health care and social care regarding the care of older people: a qualitative evidence synthesis. *Health Soc. Care Deliv. Res.* **12**, 1–87 (2024).
4. K. I. Sereti, N. B. Nguyen, P. Kamran, P. Zhao, S. Ranjbarvaziri, S. Park, S. Sabri, J. L. Engel, K. Sung, R. P. Kulkarni, Y. Ding, T. K. Hsiai, K. Plath, J. Ernst, D. Sahoo, H. K. A. Mikkola, M. L. Iruela-Arispe, R. Ardehali, Analysis of cardiomyocyte clonal expansion during mouse heart development and injury. *Nat. Commun.* **9**, 754 (2018).
5. F. A. High, J. A. Epstein, The multifaceted role of Notch in cardiac development and disease. *Nat. Rev. Genet.* **9**, 49–61 (2008).
6. G. del Monte-Nieto, M. Ramialison, A. A. S. Adam, B. Wu, A. Aharonov, G. D'uva, L. M. Bourke, M. E. Pitulescu, H. Chen, J. L. de la Pompa, W. Shou, R. H. Adams, S. K. Harten, E. Tzahor, B. Zhou, R. P. Harvey, Control of cardiac jelly dynamics by NOTCH1 and NRG1 defines the building plan for trabeculation. *Nature* **557**, 439–445 (2018).
7. J. Liao, X. Shi, "On Cardiac Elastin and Its Biomechanical Functions" in *Integration and Bridging of Multiscale Bioengineering Designs and Tissue Biomechanics*, J. Liao, J. Y. Wong, Eds. (Springer, Cham, 2025), pp. 53–86.
8. R. Bacallao, S. Sohrab, C. Phillips, "Guiding Principles of Specimen Preservation for Confocal Fluorescence Microscopy" in *Handbook of Biological Confocal Microscopy: Third Edition*, J. B. Pawley, Ed. (Springer, Boston, 2006), pp. 368–380.
9. J. T. C. Liu, A. K. Glaser, K. Bera, L. D. True, N. P. Reder, K. W. Eliceiri, A. Madabhushi, Harnessing non-destructive 3D pathology. *Nat. Biomed. Eng.* **5**, 203–218 (2021).
10. X. Xu, J. Su, R. Zhu, K. Li, X. Zhao, J. Fan, F. Mao, From morphology to single-cell molecules: high-resolution 3D histology in biomedicine. *Mol. Cancer* **24**, 63 (2025).
11. J. T. C. Liu, A. K. Glaser, C. Poudel, J. C. Vaughan, Nondestructive 3D Pathology with Light-Sheet Fluorescence Microscopy for Translational Research and Clinical Assays. *Annu. Rev. Anal. Chem.* **16**, 231–252 (2023).
12. E. H. K. Stelzer, F. Strobl, B. J. Chang, F. Preusser, S. Preibisch, K. McDole, R. Fiolka, Light sheet fluorescence microscopy. *Nat. Rev. Methods Primers* **1**, 73 (2021).
13. H.-U. Dodt, U. Leischner, A. Schierloh, N. Jährling, C. P. Mauch, K. Deininger, J. M. Deussing, M. Eder, W. Zieglgänsberger, K. Becker, Ultramicroscopy: three-dimensional visualization of neuronal networks in the whole mouse brain. *Nat. Methods* **4**, 331–336 (2007).
14. B. Migliori, M. S. Datta, C. Dupre, M. C. Apak, S. Asano, R. Gao, E. S. Boyden, O. Hermanson, R. Yuste, R. Tomer, Light sheet theta microscopy for rapid high-resolution imaging of large biological samples. *BMC Biol.* **16**, 57 (2018).
15. T. Chakraborty, M. K. Driscoll, E. Jeffery, M. M. Murphy, P. Roudot, B. J. Chang, S. Vora, W. M. Wong, C. D. Nielson, H. Zhang, V. Zhemkov, C. Hiremath, E. D. De La Cruz, Y. Yi, I. Bezprozvanny, H. Zhao, R. Tomer, R. Heintzmann, J. P. Meeks, D. K. Marciano, S. J. Morrison, G. Danuser, K. M. Dean, R. Fiolka, Light-sheet microscopy of cleared tissues with isotropic, subcellular resolution. *Nat. Methods* **16**, 1109–1113 (2019).
16. P. Fei, J. Lee, R. R. S. Packard, K. I. Sereti, H. Xu, J. Ma, Y. Ding, H. Kang, H. Chen, K.

Sung, R. Kulkarni, R. Ardehali, C. C. J. Kuo, X. Xu, C. M. Ho, T. K. Hsiai, Cardiac Light-Sheet Fluorescent Microscopy for Multi-Scale and Rapid Imaging of Architecture and Function. *Sci. Rep.* **6**, 22489 (2016).

17. S. F. Merz, S. Korste, L. Bornemann, L. Michel, P. Stock, A. Squire, C. Soun, D. R. Engel, J. Detzer, H. Lörchner, D. M. Hermann, M. Kamler, J. Klode, U. B. Hendgen-Cotta, T. Rassaf, M. Gunzer, M. Totzeck, Contemporaneous 3D characterization of acute and chronic myocardial I/R injury and response. *Nat. Commun.* **10**, 2312 (2019).
18. J. Tang, H. Zhu, X. Tian, H. Wang, S. Liu, K. Liu, H. Zhao, L. He, X. Huang, Z. Feng, Z. Ding, B. Long, Y. Yan, N. Smart, H. Gong, Q. Luo, B. Zhou, Extension of Endocardium-Derived Vessels Generate Coronary Arteries in Neonates. *Circ. Res.* **130**, 352–365 (2022).
19. T. Becher, D. F. Riascos-Bernal, D. J. Kramer, V. M. Almonte, J. Chi, T. Tong, G. H. Oliveira-Paula, I. Koleilat, W. Chen, P. Cohen, N. E. S. Sibinga, Three-Dimensional Imaging Provides Detailed Atherosclerotic Plaque Morphology and Reveals Angiogenesis After Carotid Artery Ligation. *Circ. Res.* **126**, 619–632 (2020).
20. B. C. Chen, W. R. Legant, K. Wang, L. Shao, D. E. Milkie, M. W. Davidson, C. Janetopoulos, X. S. Wu, J. A. Hammer, Z. Liu, B. P. English, Y. Mimori-Kiyosue, D. P. Romero, A. T. Ritter, J. Lippincott-Schwartz, L. Fritz-Laylin, R. D. Mullins, D. M. Mitchell, J. N. Bembenek, A. C. Reymann, R. Böhme, S. W. Grill, J. T. Wang, G. Seydoux, U. S. Tulu, D. P. Kiehart, E. Betzig, Lattice light-sheet microscopy: Imaging molecules to embryos at high spatiotemporal resolution. *Science* **346**, 1257998 (2014).
21. K. M. Dean, R. Fiolka, Uniform and scalable light-sheets generated by extended focusing. *Opt. Express* **22**, 26141–26152 (2014).
22. F. O. Fahrbach, A. Rohrbach, A line scanned light-sheet microscope with phase shaped self-reconstructing beams. *Opt. Express* **18**, 24229–24244 (2010).
23. H. Dibaji, M. N. H. Prince, Y. Yi, H. Zhao, T. Chakraborty, Axial scanning of dual focus to improve light sheet microscopy. *Biomed. Opt. Express* **13**, 4990–5003 (2022).
24. X. Guo, F. Zhao, J. Zhu, D. Zhu, Y. Zhao, P. Fei, Rapid 3D isotropic imaging of whole organ with double-ring light-sheet microscopy and self-learning side-lobe elimination. *Biomed. Opt. Express* **14**, 6206–6221 (2023).
25. K. M. Dean, P. Roudot, E. S. Welf, G. Danuser, R. Fiolka, Deconvolution-free Subcellular Imaging with Axially Swept Light Sheet Microscopy. *Biophys. J.* **108**, 2807–2815 (2015).
26. P. N. Hedde, E. Gratton, Selective Plane Illumination Microscopy with a Light Sheet of Uniform Thickness Formed by an Electrically Tunable Lens. *Microsc. Res. Tech.* **81**, 924–928 (2018).
27. F. F. Voigt, D. Kirschenbaum, E. Platonova, S. Pagès, R. A. A. Campbell, R. Kastli, M. Schaettin, L. Egolf, A. van der Bourg, P. Bethge, K. Haenraets, N. Frézel, T. Topilko, P. Perin, D. Hillier, S. Hildebrand, A. Schueth, A. Roebroeck, B. Roska, E. T. Stoeckli, R. Pizzala, N. Renier, H. U. Zeilhofer, T. Karayannis, U. Ziegler, L. Batti, A. Holtmaat, C. Lüscher, A. Aguzzi, F. Helmchen, The mesoSPIM initiative: open-source light-sheet microscopes for imaging cleared tissue. *Nat. Methods* **16**, 1105–1108 (2019).
28. N. Renier, Z. Wu, D. J. Simon, J. Yang, P. Ariel, M. Tessier-Lavigne, iDISCO: A Simple, Rapid Method to Immunolabel Large Tissue Samples for Volume Imaging. *Cell* **159**, 896–910 (2014).
29. D. S. Richardson, J. W. Lichtman, Clarifying Tissue Clearing. *Cell* **162**, 246–257 (2015).
30. V. V Tuchin, Optical clearing of tissues and blood using the immersion method. *J. Phys. D: Appl. Phys.* **38**, 2497–2518 (2005).
31. Z. Ou, Y. S. Duh, N. J. Rommelfanger, C. H. C. Keck, S. Jiang, K. Brinson, S. Zhao, E. L. Schmidt, X. Wu, F. Yang, B. Cai, H. Cui, W. Qi, S. Wu, A. Tantry, R. Roth, J. Ding, X. Chen, J. A. Kaltschmidt, M. L. Brongersma, G. Hong, Achieving optical transparency in live animals with absorbing molecules. *Science* **385**, eadm6869 (2024).

32. E. Remacha, L. Friedrich, J. Vermot, F. O. Fahrbach, How to define and optimize axial resolution in light-sheet microscopy: a simulation-based approach. *Biomed. Opt. Express* **11**, 8–26 (2019).
33. E. J. Botcherby, R. Juskaitis, M. J. Booth, T. Wilson, Aberration-free optical refocusing in high numerical aperture microscopy. *Opt. Lett.* **32**, 2007–2009 (2007).
34. E. J. Botcherby, R. Juškaitis, M. J. Booth, T. Wilson, An optical technique for remote focusing in microscopy. *Opt. Commun.* **281**, 880–887 (2008).
35. O. Sodimu, M. Almasian, P. Gan, S. Hassan, X. Zhang, N. Liu, Y. Ding, Light sheet imaging and interactive analysis of the cardiac structure in neonatal mice. *J. Biophotonics* **16**, e202200278 (2023).
36. R. Tomer, M. Lovett-Barron, I. Kauvar, A. Andalman, V. M. Burns, S. Sankaran, L. Grosenick, M. Broxton, S. Yang, K. Deisseroth, SPED Light Sheet Microscopy: Fast Mapping of Biological System Structure and Function. *Cell* **163**, 1796–1806 (2015).
37. J. Brewer, M. Almasian, A. Saberigarakani, X. Zhang, F. Shi, Y. Ding, Resolution enhancement by subpixel sampling and computational reconstruction. *Opt. Lett.* **50**, 2457–2460 (2025).
38. K. N. Kirchner, H. Li, A. R. Denton, S. B. Harrod, C. F. Mactutus, R. M. Booze, A hydrophobic tissue clearing method for rat brain tissue. *J. Vis. Exp.* **166**, e61821 (2020).
39. L. A. Royer, W. C. Lemon, R. K. Chhetri, Y. Wan, M. Coleman, E. W. Myers, P. J. Keller, Adaptive light-sheet microscopy for long-term, high-resolution imaging in living organisms. *Nat. Biotechnol.* **34**, 1267–1278 (2016).
40. J. B. Wheeler, R. Mukherjee, R. E. Stroud, J. A. Jones, J. S. Ikonomidis, Relation of murine thoracic aortic structural and cellular changes with aging to passive and active mechanical properties. *J. Am. Heart Assoc.* **4**, e001744 (2015).
41. B. Trachet, A. Piersigilli, R. A. Fraga-Silva, L. Aslanidou, J. Sordet-Dessimoz, A. Astolfo, M. F. M. Stampanoni, P. Segers, N. Stergiopulos, Ascending Aortic Aneurysm in Angiotensin II-Infused Mice: Formation, Progression, and the Role of Focal Dissections. *Arterioscler. Thromb. Vasc. Biol.* **36**, 673–681 (2016).
42. D. Stalling, M. Westerhoff, H. C. Hege, "amira: A Highly Interactive System for Visual Data Analysis" in *Visualization Handbook*, C. D. Hansen, C. R. Johnson, Eds. (Butterworth-Heinemann, Burlington, 2005), pp. 749–767.
43. N. G. Frangogiannis, The extracellular matrix in myocardial injury, repair, and remodeling. *J. Clin. Invest.* **127**, 1600–1612 (2017).
44. X. Wang, S. Yu, L. Xie, M. Xiang, H. Ma, The role of the extracellular matrix in cardiac regeneration. *Heliyon* **11**, e41157 (2025).
45. K. P. Rommel, M. Von Roeder, K. Latuscynski, C. Oberueck, S. Blazek, K. Fengler, C. Besler, M. Sandri, C. Lücke, M. Gutberlet, A. Linke, G. Schuler, P. Lurz, Extracellular Volume Fraction for Characterization of Patients With Heart Failure and Preserved Ejection Fraction. *J. Am. Coll. Cardiol.* **67**, 1815–1825 (2016).
46. J. J. Pagano, D. Yim, C. Z. Lam, S. J. Yoo, M. Seed, L. Grosse-Wortmann, Normative data for myocardial native T1 and extracellular volume fraction in children. *Radiol. Cardiothorac. Imaging* **2**, e190234 (2020).
47. P. E. Rios Coronado, K. Red-Horse, Enhancing cardiovascular research with whole organ imaging. *Curr. Opin. Hematol.* **28**, 214–220 (2021).
48. C. C. Chang, A. Chu, S. Meyer, Y. Ding, M. M. Sun, P. Abiri, K. I. Baek, V. Gudapati, X. Ding, P. Guihard, K. I. Bostrom, S. Li, L. K. Gordon, J. J. Zheng, T. K. Hsiai, Three-dimensional Imaging Coupled with Topological Quantification Uncovers Retinal Vascular Plexuses Undergoing Obliteration. *Theranostics* **11**, 1162–1175 (2021).
49. E. Bullmore, O. Sporns, Complex brain networks: graph theoretical analysis of structural and functional systems. *Nat. Rev. Neurosci.* **10**, 186–198 (2009).

50. S. Anbazhakan, P. E. Rios Coronado, A. N. L. Sy-Quia, L. W. Seow, A. M. Hands, M. Zhao, M. L. Dong, M. R. Pfaller, Z. A. Amir, B. C. Raftrey, C. K. Cook, G. D'Amato, X. Fan, I. M. Williams, S. K. Jha, D. Bernstein, K. Nieman, A. M. Pa□ca, A. L. Marsden, K. Red Horse, Blood flow modeling reveals improved collateral artery performance during the regenerative period in mammalian hearts. *Nat. Cardiovasc. Res.* **1**, 775–790 (2022).
51. M. Almasian, X. Zhang, A. Saberigarakani, Y. Ding, "Multi-scale Light-Sheet Imaging for Volumetric Assessment of Cardiovascular Architecture and Function" in *Integration and Bridging of Multiscale Bioengineering Designs and Tissue Biomechanics*, J. Liao, J. Y. Wong, Eds. (Springer, Cham, 2025), pp. 501–520.
52. H. Xie, X. Han, G. Xiao, H. Xu, Y. Zhang, G. Zhang, Q. Li, J. He, D. Zhu, X. Yu, Q. Dai, Multifocal fluorescence video-rate imaging of centimetre-wide arbitrarily shaped brain surfaces at micrometric resolution. *Nat. Biomed. Eng.* **8**, 740–753 (2024).
53. P. Liu, T. Zhu, Y. Li, R. Zhao, Q. Wang, H. Yang, H. Ma, X. Mu, H. Wang, G. Feng, X. D. Zhang, D. Ming, Systematic and quantitative comparison of axially overlapped multi-focus and Gaussian light sheets. *Opt. Lasers Eng.* **181**, 108355 (2024).
54. H. Li, Z. Wu, Z. Yang, K. Zhanghao, P. Xi, D. Jin, Axially overlapped multi-focus light sheet with enlarged field of view. *Appl. Phys. Lett.* **118**, 223701 (2021).
55. P. Fei, J. Nie, J. Lee, Y. Ding, S. Li, H. Zhang, M. Hagiwara, T. Yu, T. Segura, C. M. Ho, D. Zhu, T. K. Hsiai, Subvoxel light-sheet microscopy for high-resolution high-throughput volumetric imaging of large biomedical specimens. *Adv. Photon.* **1**, 016002 (2019).
56. J. Huisken, E. H. K. Stelzer, J. Swoger, P. Verveer, K. Greger, Multi-view image fusion improves resolution in three-dimensional microscopy. *Opt. Express* **15**, 8029–8042 (2007).
57. M. Almasian, A. Saberigarakani, X. Zhang, B. Lee, Y. Ding, Light-sheet Imaging to Reveal Cardiac Structure in Rodent Hearts. *J. Vis. Exp.* **205**, e66707 (2024).
58. R. McGorty, H. Liu, D. Kamiyama, Z. Dong, S. Guo, B. Huang, Open-top selective plane illumination microscope for conventionally mounted specimens. *Opt. Express* **23**, 16142–16153 (2015).
59. A. K. Glaser, K. W. Bishop, L. A. Barner, E. A. Susaki, S. I. Kubota, G. Gao, R. B. Serafin, P. Balaram, E. Turschak, P. R. Nicovich, H. Lai, L. A. G. Lucas, Y. Yi, E. K. Nichols, H. Huang, N. P. Reder, J. J. Wilson, R. Sivakumar, E. Shamskhou, C. R. Stoltzfus, X. Wei, A. K. Hempton, M. Pende, P. Murawala, H. U. Dodt, T. Imaizumi, J. Shendure, B. J. Beliveau, M. Y. Gerner, L. Xin, H. Zhao, L. D. True, R. C. Reid, J. Chandrashekar, H. R. Ueda, K. Svoboda, J. T. C. Liu, A hybrid open-top light-sheet microscope for versatile multi-scale imaging of cleared tissues. *Nat. Methods* **19**, 613–619 (2022).
60. A. H. Song, M. Williams, D. F. K. Williamson, S. S. L. Chow, G. Jaume, G. Gao, A. Zhang, B. Chen, A. S. Baras, R. Serafin, R. Colling, M. R. Downes, X. Farré, P. Humphrey, C. Verrill, L. D. True, A. V. Parwani, J. T. C. Liu, F. Mahmood, Analysis of 3D pathology samples using weakly supervised AI. *Cell* **187**, 2502–2520.e17 (2024).
61. Y. Ding, V. Gudapati, R. Lin, Y. Fei, R. R. S. Packard, S. Song, C. C. Chang, K. I. Baek, Z. Wang, M. Roustaei, D. Kuang, C. C. J. Kuo, T. K. Hsiai, Saak Transform-Based Machine Learning for Light-Sheet Imaging of Cardiac Trabeculation. *IEEE Trans. Biomed. Eng.* **68**, 225–235 (2020).
62. Y. Rivenson, H. Wang, Z. Wei, K. de Haan, Y. Zhang, Y. Wu, H. Günaydın, J. E. Zuckerman, T. Chong, A. E. Sisk, L. M. Westbrook, W. D. Wallace, A. Ozcan, Virtual histological staining of unlabelled tissue-autofluorescence images via deep learning. *Nat. Biomed. Eng.* **3**, 466–477 (2019).
63. Y. Ding, A. Abiri, P. Abiri, S. Li, C. C. Chang, K. I. Baek, J. J. Hsu, E. Sideris, Y. Li, J. Lee, T. Segura, T. P. Nguyen, A. Bui, R. R. Sevag Packard, P. Fei, T. K. Hsiai, Integrating light-sheet imaging with virtual reality to recapitulate developmental cardiac mechanics.

JCI Insight **2**, e97180 (2017).
64. J. Yuan, S. S. Hassan, J. Wu, C. R. Koger, R. R. S. Packard, F. Shi, B. Fei, Y. Ding, Extended reality for biomedicine. *Nat. Rev. Methods Primers* **3**, 14 (2023).
65. H. Peng, J. Tang, H. Xiao, A. Bria, J. Zhou, V. Butler, Z. Zhou, P. T. Gonzalez-Bellido, S. W. Oh, J. Chen, A. Mitra, R. W. Tsien, H. Zeng, G. A. Ascoli, G. Iannello, M. Hawrylycz, E. Myers, F. Long, Virtual finger boosts three-dimensional imaging and microsurgery as well as terabyte volume image visualization and analysis. *Nat. Commun.* **5**, 4342 (2014).
66. D. Kaltenecker, R. Al-Maskari, M. Negwer, L. Hoeher, F. Kofler, S. Zhao, M. Todorov, Z. Rong, J. C. Paetzold, B. Wiestler, M. Piraud, D. Rueckert, J. Geppert, P. Morigny, M. Rohm, B. H. Menze, S. Herzig, M. Berriel Diaz, A. Ertürk, Virtual reality-empowered deep-learning analysis of brain cells. *Nat. Methods* **21**, 1306–1315 (2024).
67. D. Hörl, F. Rojas Rusak, F. Preusser, P. Tillberg, N. Randel, R. K. Chhetri, A. Cardona, P. J. Keller, H. Harz, H. Leonhardt, M. Treier, S. Preibisch, BigStitcher: reconstructing high-resolution image datasets of cleared and expanded samples. *Nat. Methods* **16**, 870–874 (2019).
68. J. Schindelin, I. Arganda-Carreras, E. Frise, V. Kaynig, M. Longair, T. Pietzsch, S. Preibisch, C. Rueden, S. Saalfeld, B. Schmid, J. Y. Tinevez, D. J. White, V. Hartenstein, K. Eliceiri, P. Tomancak, A. Cardona, Fiji: an open-source platform for biological-image analysis. *Nat. Methods* **9**, 676–682 (2012).
69. C. A. Schneider, W. S. Rasband, K. W. Eliceiri, NIH Image to ImageJ: 25 years of image analysis. *Nat. Methods* **9**, 671–675 (2012).
70. K. M. Dean, T. Chakraborty, S. Daetwyler, J. Lin, G. Garrelts, O. M'Saad, H. T. Mekbib, F. F. Voigt, M. Schaettin, E. T. Stoeckli, F. Helmchen, J. Bewersdorf, R. Fiolka, Isotropic imaging across spatial scales with axially swept light-sheet microscopy. *Nat. Protoc.* **17**, 2025–2053 (2022).
71. T. Yardeni, M. Eckhaus, H. D. Morris, M. Huizing, S. Hoogstraten-Miller, Retro-orbital injections in mice. *Lab Anim.* **40**, 155–160 (2011).
72. A. F. Frangi, W. J. Niessen, K. L. Vincken, M. A. Viergever, "Multiscale vessel enhancement filtering" in *Medical Image Computing and Computer-Assisted Intervention — MICCAI 1998*, W. M. Wells, A. Colchester, S. Delp, Eds. (Springer, Berlin, 1998), pp. 130–137.
73. D. Lesage, E. D. Angelini, I. Bloch, G. Funka-Lea, A review of 3D vessel lumen segmentation techniques: Models, features and extraction schemes. *Med. Image Anal.* **13**, 819–845 (2009).
74. J. M. Singelyn, J. A. DeQuach, S. B. Seif-Naraghi, R. B. Littlefield, P. J. Schup-Magoffin, K. L. Christman, Naturally derived myocardial matrix as an injectable scaffold for cardiac tissue engineering. *Biomaterials* **30**, 5409–5416 (2009).
75. E. Mulvany, S. McMahan, J. Xu, N. Yazdani, R. Willits, J. Liao, G. Zhang, Y. Hong, In vitro comparison of harvesting site effects on cardiac extracellular matrix hydrogels. *J. Biomed. Mater. Res.* **109**, 1922–1930 (2021).
76. E. Kugler, T. Chico, P. Armitage, "Image analysis in light sheet fluorescence microscopy images of transgenic zebrafish vascular development" in *Medical Image Understanding and Analysis*, M. Nixon, S. Mahmoodi, R. Zwiggelaar, Eds. (Springer, Cham, 2018), pp. 343–353.
77. M. Barthélemy, Spatial networks. *Phys. Rep.* **499**, 1–101 (2011).
78. X. Kong, Y. Shi, S. Yu, J. Liu, F. Xia, Academic social networks: Modeling, analysis, mining and applications. *J. Netw. Comput. Appl.* **132**, 86–103 (2019).
79. Z. Wang, A. C. Bovik, H. R. Sheikh, E. P. Simoncelli, Image quality assessment: From error visibility to structural similarity. *IEEE Trans. Image Process.* **13**, 600–612 (2004).

Acknowledgments

We express our gratitude to Dr. Fenghua Shi for valuable discussions on simulation at UT□Dallas. We also appreciate the constructive comments and technical support provided by the D□Incubator members at UT□Dallas.

Funding:
National Institutes of Health grant R00HL148493 (YD)
National Institutes of Health grant R01HL162635 (YD)
National Science Foundation grant 2503230 (YD)
Cecil H. and Ida Green Professorship in Systems Biology Science (YD)

Author contributions:
Conceptualization: – MA, YD
Methodology: – MA, AS, JB, YD
Software: – MA, AS, JB, RH, YD
Validation: – MA, AS, JB, XZ, RH, YL, SW, JL, MW, DT, YD
Formal analysis: – MA, AS, JB, XZ, RH, HH, YD
Investigation: – MA, YL, SW, JL, YH, MW, DT, DS, YD
Resources: – MA, YL, SW, YW, JL, YH, MW, DT, DS, YD
Data curation: – MA, AS, JB, XZ, RH, HH, YD
Writing – original draft: – MA, JB, YL, YW, YH, MW, YD
Writing – review & editing: – MA, AS, JB, JC, SW, HH, DT, YD
Visualization: MA, AS, JB, YD
Supervision: YD
Project administration: YD
Funding acquisition: YD

Competing interests: Authors declare that they have no competing interests.

Data and materials availability: All data are available in the main text or the supplementary materials. Datasets supporting the findings of this study, MATLAB codes, and software for calculating AS-DiLS are publicly available on Zenodo at https://doi.org/10.5281/zenodo.17216456. Additional information required to reanalyze the data reported in this paper is available from the corresponding author upon request.

Figures and Tables

Fig. 1. Dithered and axially swept dithered light-sheet microscopy. (A) Conventional LSM schematic showing the trade-off between light-sheet thickness (2ω) and confocal region (CR). **(B)** DiLS extends the CR by dithering the light-sheet along its propagation direction, generating a time-averaged beam. **(C)** Experimental profiles of static and dithered light-sheets with 50, 100, and 200 µm ranges in 50 µM fluorescein solution. **(D)** Thickness variations along the propagation axis quantified by FWHM. **(E)** Normalized intensity profiles as a function of dithering range. **(F)** Quantification of average light-sheet thickness in the CR (orange) and the extended CR (blue) as functions of the dithering range, showing optimal extension below the $2\sqrt{2}\omega$ threshold. **(G)** Concept of AS-DiLS integrating DiLS with axial sweeping to cover the full imaging plane. **(H)** Scanning mechanism with the extended CR synchronized to the rolling shutter of the sCMOS camera. **(I)** Illumination profile in fluorescein solution, sampled at left, middle, and right regions, each spanning 195 µm. **(J)** Quantification of normalized intensity across three positions (one-way ANOVA, $p = 0.28$), confirming uniform distribution across the imaging plane. Px, camera pixel size; M, magnification; FOV, field of view; ET, exposure time. Scale bars: **(C)** 100 µm, **(I)** 2 mm and 50 µm (insets).

Fig. 2. Comparative analysis of imaging performance in LSM, DiLS, and AS-DiLS. Volumetric imaging of 0.53 µm fluorescent beads in 1% agarose gel using conventional LSM **(A)**, DiLS **(B),** and AS-DiLS **(C)**. Cropped volumes of 700 × 700 × 250 μm^3 shown for LSM and DiLS; dashed box in **(C)** marks the crop region. Maximum intensity projections (MIP) of XY and YZ views displayed in Fire pseudo color. Insets show selected beads at different positions used for resolution analysis. Three beads located at different positions were selected for lateral and axial resolution analysis for LSM, DiLS, and AS-DiLS. Lateral (blue) and axial (red) intensity profiles were fit with Gaussian distributions, and FWHM values calculated. For all beads within confocal region (n = 103 for LSM, n = 115 for DiLS, and n = 1579 for AS-DiLS), the average FWHM and standard deviation along the x, y, and z axes were computed and tabulated. In AS-DiLS, beads at the far left and right of the 1800 × 1800 μm^2 image were also analyzed. Scale bars: 200 µm (XY and YZ views) and 5 µm (bead insets).

Fig. 3. Mouse heart clearing and quantitative evaluation of AS-DiLS images. (A) Schematic of iDISCO-based clearing protocol adapted for autofluorescence and immunofluorescence imaging of intact mouse hearts. **(B)** Heart embedding in agarose and subsequent clearing in refractive index matching. **(C)** Imaging uniformity assessed by acquiring the same region of the heart in six adjacent lateral sections across the FOV. **(D)** SSIM values between adjacent tiles ranged from 0.96 to 0.99, confirming consistent performance across the imaging plane. **(E)** Comparison of image quality in 2D cross section between LSM (left) and AS-DiLS (right). Three representative 1 × 1 mm regions (green, orange, and purple boxes) from the left, middle, and right portions of the heart were selected for quantitative analysis. **(F)** Normalized intensity profiles for each region, with SBR and CNR values reported. **(G)** First-derivative plots of intensity profiles comparing LSM and AS-DiLS showed sharper edges with AS-DiLS. **(H)** Fourier transform analysis of representative regions revealed a larger cut-off radius in AS-DiLS, reflecting improved support of lower-bound spatial frequencies. Grid line in **(B)** 5 mm. Scale bars: **(C)** 200 µm, **(E)** 1 mm and 200 µm (insets).

Fig. 4. Autofluorescence imaging and in-depth morphological analysis. (A) Schematic representation of the light-sheet imaging setup for intact adult heart volumetric imaging. **(B)** Representative 2D cross-section at a depth of 2350 µm. **(C)** 3D volumetric reconstruction processed with zoomed views resolving trabeculae, fibers, and vessel morphology. **(D)** Pipeline for tracing and segmentation of coronary arteries. **(E)** Quantitative vascular morphology of the coronary artery network, including branch count and lumen diameter, with a color-coded diameter map. **(F)** Volumetric reconstruction of a decellularized adult rat heart imaged under 2× magnification using a tiled acquisition. Autofluorescence from extracellular matrix enables label-free visualization of structures throughout the tissue. **(G)** AS-DiLS imaging of extracellular matrix in a decellularized left ventricle of a porcine heart. RA, right atrium; LA, left atrium; RV, right ventricle; LV, left ventricle; MV, mitral valve; AV, aortic valve; RCA, right coronary artery; LCA, left coronary artery; SpA, septal artery. Scale bars: 1 mm and 200 µm (insets).

Fig. 5. Volumetric immunostaining imaging and topological analysis of the intact neonatal and embryonic mouse heart. (A, B) 2D images of a P7 heart in long (depth of 960 µm) and short axes after in vivo retro-orbital injection of Alexa Fluor 594 conjugated anti-mouse CD31 to label endothelial cells. **(C)** MIP integrated across 345 µm depth shows uniform vascular labeling and clear delineation of the LCA and SpA from the aorta to distal branches. **(D)** Quantitative 3D analysis of capillaries using vessel tracing in Amira. Reconstructions from three CD31-labeled P7 hearts (n = 3) were used to calculate vessel length density (VLD) in three 200 × 200 × 400 μm^3 sub-volumes, with group statistics reported. **(E)** Volumetric imaging of embryonic hearts at E14.5, E15.5, and E16.5 immunostained with PECAM/Endomucin (Rat-568) and cleared using iDISCO. MIP of E15.5 shows coronary vessel formation. Segmented graphs enabled calculation of Euler characteristics and clustering coefficients across four regions per heart. The centerline and error bars in **(D)** denote the mean and standard deviation, with the associated data points plotted. *P* values were calculated using Student's *t*-test. RVW, right ventricular wall; LVW, left ventricular wall; IVS, interventricular septum. Scale bars: 1 mm and 200 µm (insets).

Supplementary Materials

The file includes:
Supplementary Notes S1 to S3
Figs. S1 to S17
Table S1
Legends for movies S1 to S6
References

Other Supplementary Material for this manuscript includes the following:
Movies S1 to S6

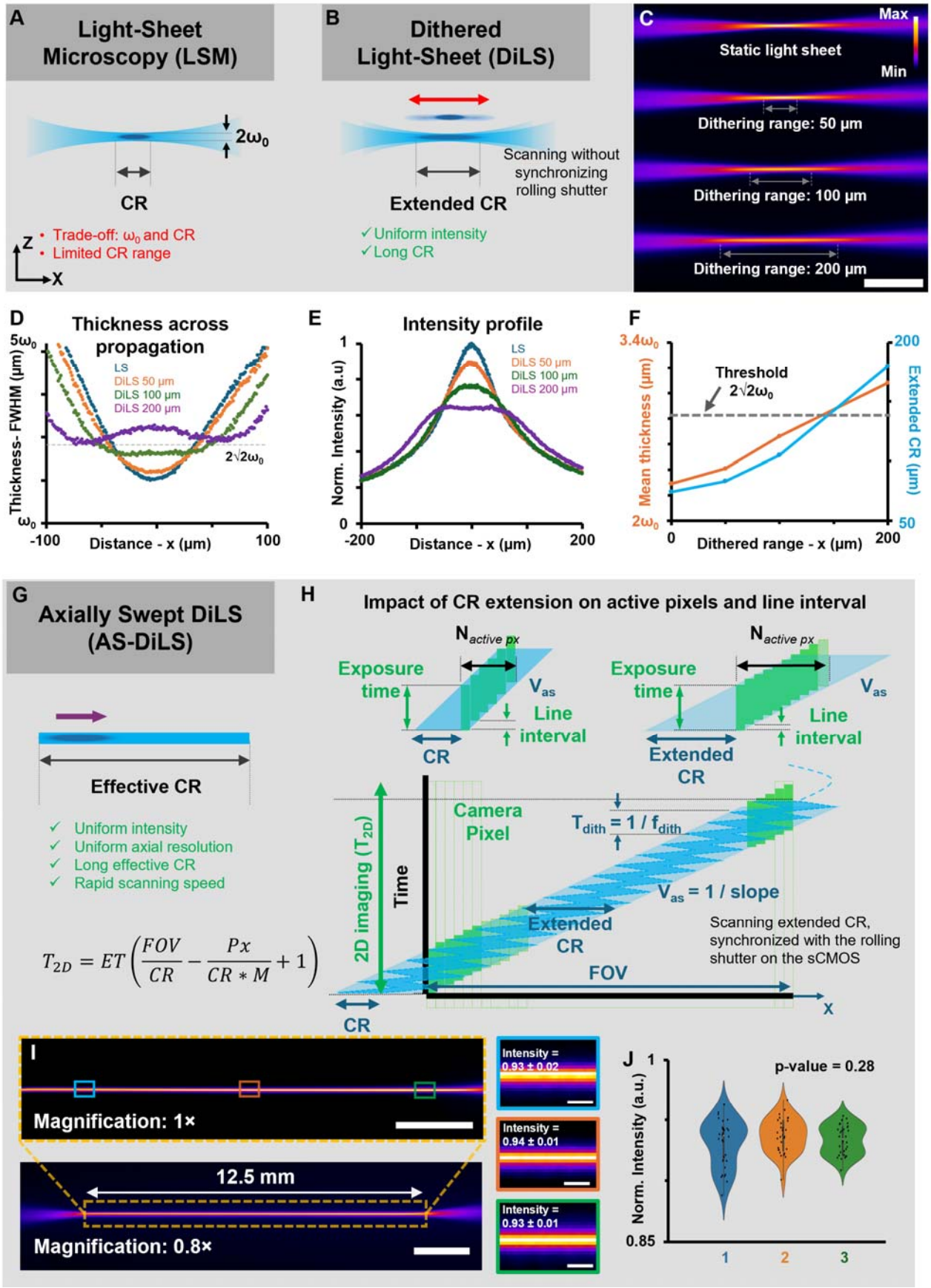
A
Light-Sheet Microscopy (LSM)
2ω0
CR
• Trade-off: ω0 and CR
• Limited CR range
Z
X
B
Dithered Light-Sheet (DiLS)
Scanning without synchronizing rolling shutter
Extended CR
✓Uniform intensity
✓Long CR
C
Max
Min
Static light sheet
Dithering range: 50 µm
Dithering range: 100 µm
Dithering range: 200 µm
D
Thickness across propagation
5ω0
ω0
Thickness- FWHM (µm)
LS
DiLS 50 µm
DiLS 100 µm
DiLS 200 µm
2√2ω0
-100
Distance - x (µm)
100
E
Intensity profile
1
0
Norm. Intensity (a.u)
LS
DiLS 50 µm
DiLS 100 µm
DiLS 200 µm
-200
Distance - x (µm)
200
F
3.4ω0
2ω0
Mean thickness (µm)
Threshold
2√2ω0
200
50
Extended CR (µm)
0
Dithered range - x (µm)
200
G
Axially Swept DiLS (AS-DiLS)
Effective CR
✓ Uniform intensity
✓ Uniform axial resolution
✓ Long effective CR
✓ Rapid scanning speed
$T_{2D} = ET\left(\frac{FOV}{CR} - \frac{Px}{CR * M} + 1\right)$
H
Impact of CR extension on active pixels and line interval
N active px
Exposure time
Vas
Line interval
CR
N active px
Exposure time
Vas
Line interval
Extended CR
Camera Pixel
Tdith = 1 / fdith
2D imaging (T2D)
Time
Vas = 1 / slope
Extended CR
Scanning extended CR, synchronized with the rolling shutter on the sCMOS
FOV
CR
X
I
Magnification: 1×
12.5 mm
Magnification: 0.8×
Intensity = 0.93 ± 0.02
Intensity = 0.94 ± 0.01
Intensity = 0.93 ± 0.01
J
1
0.85
Norm. Intensity (a.u.)
p-value = 0.28
1
2
3

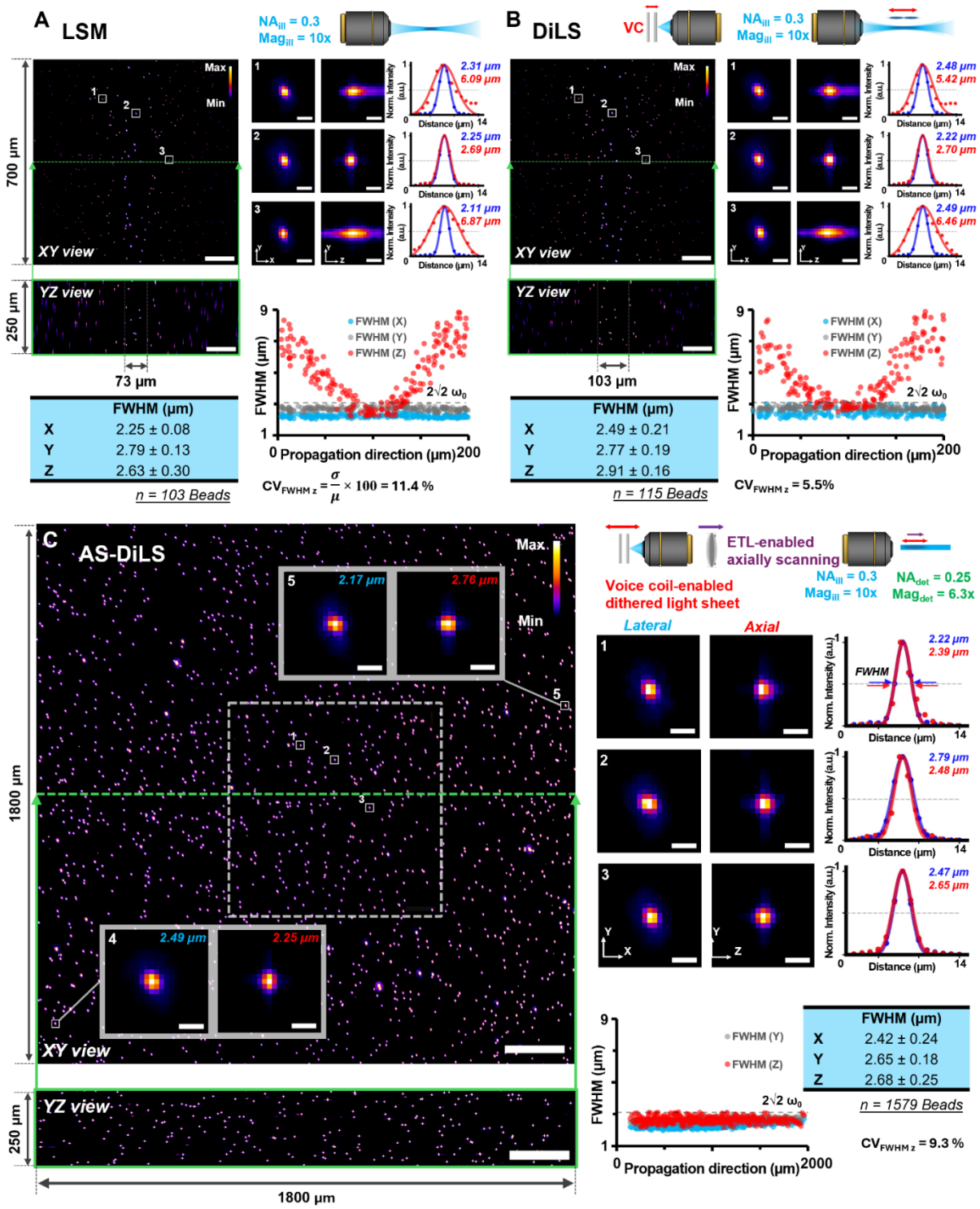
A LSM
NA_ill = 0.3
Mag_ill = 10x
700 µm
250 µm
XY view
YZ view
73 µm
FWHM (µm)
X 2.25 ± 0.08
Y 2.79 ± 0.13
Z 2.63 ± 0.30
n = 103 Beads
CV_FWHM z = σ/μ × 100 = 11.4 %
FWHM (X)
FWHM (Y)
FWHM (Z)
2√2 ω0
Propagation direction (µm)
B DiLS
VC
NA_ill = 0.3
Mag_ill = 10x
103 µm
FWHM (µm)
X 2.49 ± 0.21
Y 2.77 ± 0.19
Z 2.91 ± 0.16
n = 115 Beads
CV_FWHM z = 5.5%
C AS-DiLS
1800 µm
250 µm
1800 µm
ETL-enabled axially scanning
Voice coil-enabled dithered light sheet
NA_ill = 0.3
Mag_ill = 10x
NA_det = 0.25
Mag_det = 6.3x
Lateral
Axial
FWHM
Norm. Intensity (a.u.)
Distance (µm)
FWHM (µm)
X 2.42 ± 0.24
Y 2.65 ± 0.18
Z 2.68 ± 0.25
n = 1579 Beads
CV_FWHM z = 9.3 %

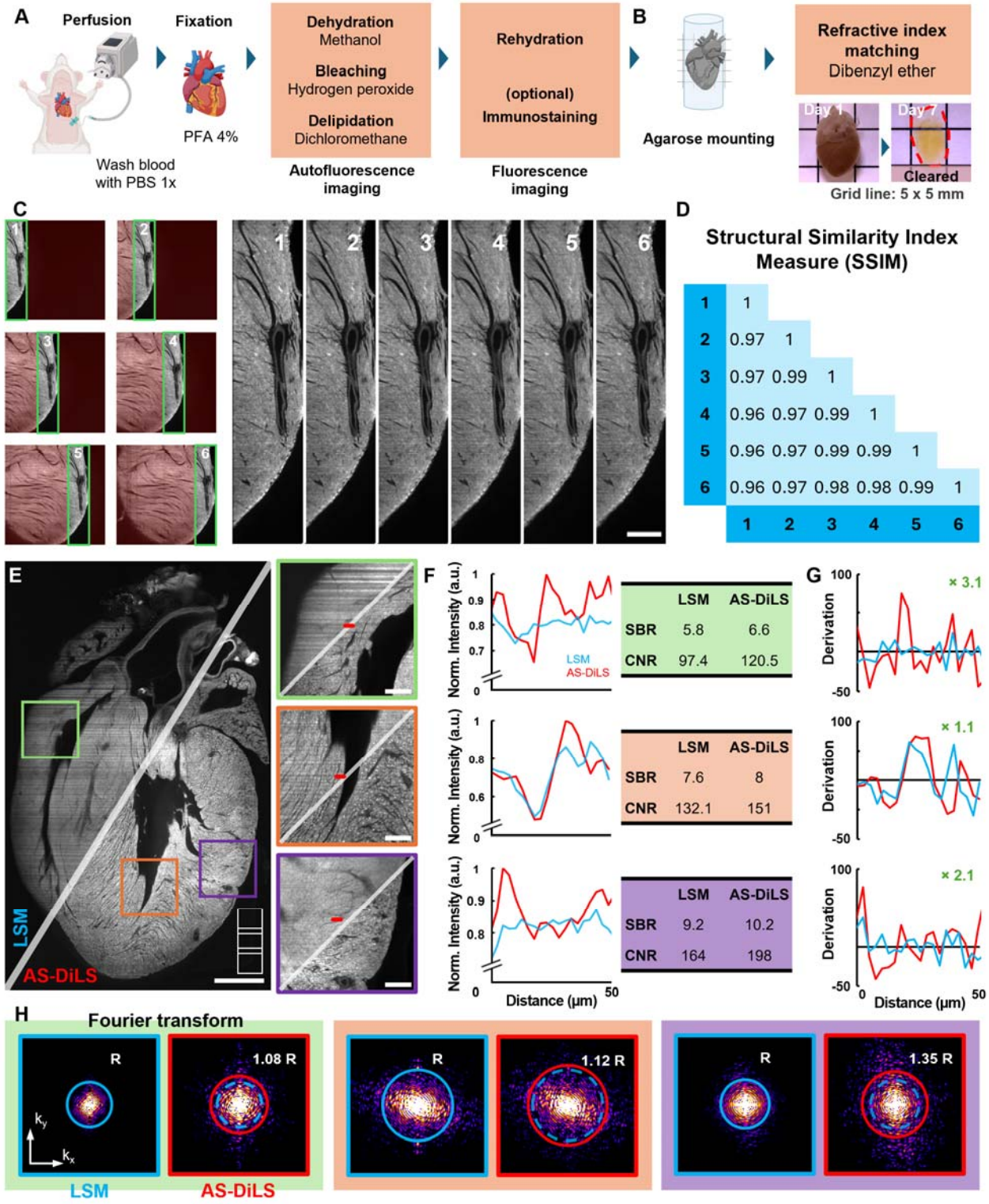
A
Perfusion
Fixation
Wash blood with PBS 1x
PFA 4%
Dehydration
Methanol
Bleaching
Hydrogen peroxide
Delipidation
Dichloromethane
Autofluorescence imaging
Rehydration
(optional)
Immunostaining
Fluorescence imaging
B
Agarose mounting
Refractive index matching
Dibenzyl ether
Day 1
Day 7
Cleared
Grid line: 5 x 5 mm
C
D
Structural Similarity Index Measure (SSIM)
1 1
2 0.97 1
3 0.97 0.99 1
4 0.96 0.97 0.99 1
5 0.96 0.97 0.99 0.99 1
6 0.96 0.97 0.98 0.98 0.99 1
1 2 3 4 5 6
E
LSM
AS-DiLS
F
Norm. Intensity (a.u.)
LSM
AS-DiLS
Distance (µm)
LSM AS-DiLS
SBR 5.8 6.6
CNR 97.4 120.5
LSM AS-DiLS
SBR 7.6 8
CNR 132.1 151
LSM AS-DiLS
SBR 9.2 10.2
CNR 164 198
G
Derivation
× 3.1
× 1.1
× 2.1
Distance (µm)
H
Fourier transform
R
1.08 R
1.12 R
1.35 R
LSM
AS-DiLS

116

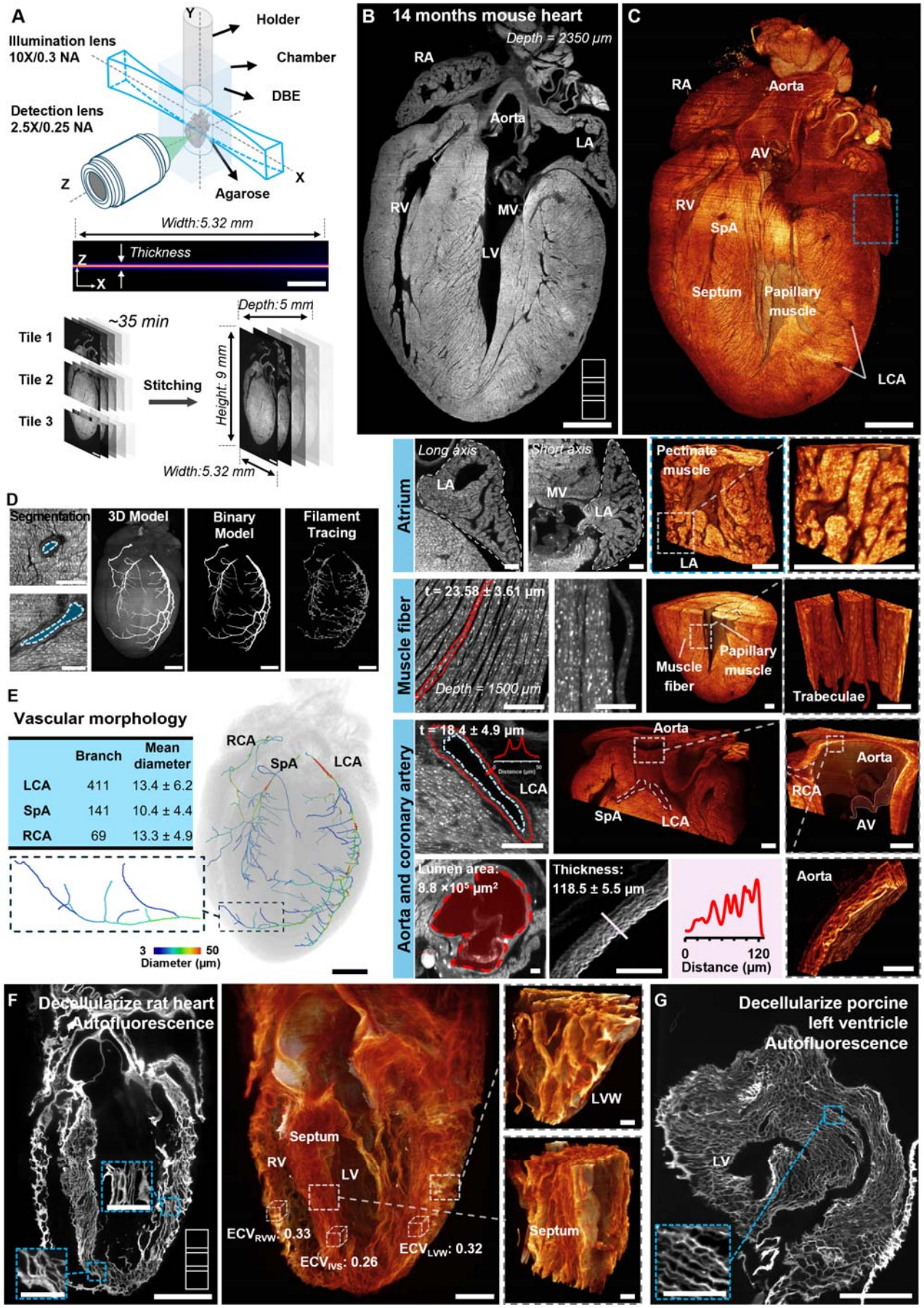
A
Illumination lens
10X/0.3 NA
Holder
Chamber
DBE
Detection lens
2.5X/0.25 NA
Agarose
Width:5.32 mm
Thickness
~35 min
Tile 1
Tile 2
Tile 3
Stitching
Depth:5 mm
Height: 9 mm
Width:5.32 mm
B 14 months mouse heart
Depth = 2350 μm
RA
Aorta
LA
RV
MV
LV
C
RA
Aorta
AV
RV
SpA
Septum
Papillary muscle
LCA
Atrium
Long axis
Short axis
LA
MV
Pectinate muscle
Muscle fiber
t = 23.58 ± 3.61 μm
Depth = 1500 μm
Papillary muscle
Trabeculae
Aorta and coronary artery
t = 18.4 ± 4.9 μm
LCA
Aorta
SpA
RCA
AV
Lumen area:
8.8 ×10⁵ μm²
Thickness:
118.5 ± 5.5 μm
0
120
Distance (μm)
D
Segmentation
3D Model
Binary Model
Filament Tracing
E
Vascular morphology
Branch
Mean diameter
LCA 411 13.4 ± 6.2
SpA 141 10.4 ± 4.4
RCA 69 13.3 ± 4.9
RCA
SpA
LCA
3
50
Diameter (μm)
F Decellularize rat heart
Autofluorescence
Septum
RV
LV
ECV_RVW: 0.33
ECV_IVS: 0.26
ECV_LVW: 0.32
LVW
Septum
G Decellularize porcine
left ventricle
Autofluorescence
LV

117

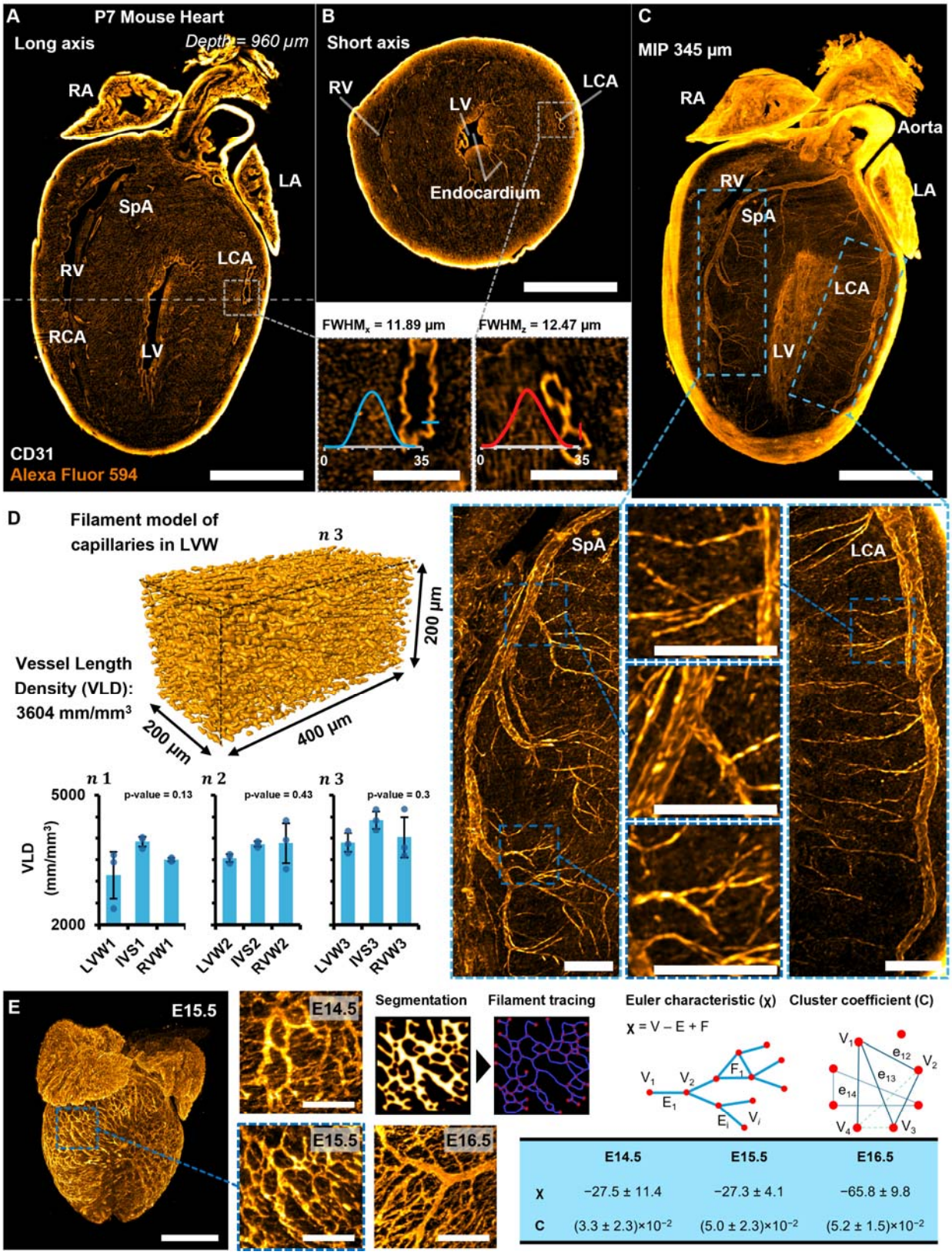

	E14.5	E15.5	E16.5
χ	−27.5 ± 11.4	−27.3 ± 4.1	−65.8 ± 9.8
C	(3.3 ± 2.3)×10⁻²	(5.0 ± 2.3)×10⁻²	(5.2 ± 1.5)×10⁻²